DETECTION AND SIMULATION OF DELAYED γ-RAYS FROM PHOTOFISSION

by

John George Kavouras

A thesis submitted to the faculty of
The University of Utah
in partial fulfillment of the requirements for the degree of

Master of Science

in

Nuclear Engineering

Department of Civil and Environmental Engineering

The University of Utah

May 2014

The University of Utah Graduate School

STATEMENT OF THESIS APPROVAL

The thesis of **John George Kavouras**

has been approved by the following supervisory committee members:

Tatjana Jevremovic	, Chair	**3/7/14** Date Approved
Luther McDonald IV	, Member	**3/7/14** Date Approved
Hermilo Hernandez	, Member	**3/7/14** Date Approved

and by **Michael Barber** , Chair/Dean of

the Department/College/School of **Civil and Environmental Engineering**

and by David B. Kieda, Dean of The Graduate School.

ABSTRACT

Discrimination of delayed emissions from photonuclear fission events provides the necessary information for the detection of nuclear materials. The time and energy characteristics of signature signals provide unique fingerprints which can be used for the identification and quantification of fissionable isotopes using γ-ray spectroscopy. This investigation explores measurement results of β-delayed γ-rays from photofission events. During the experiment, spectroscopy measurements were taken using two high-purity germanium detectors while three separate signal processing units were used for data acquisition. Interrogation of ^{238}U, ^{239}Pu, and ^{232}Th was performed using a 22 MeV pulsed bremsstrahlung photon beam. Fission fragments with energies above 3 MeV were identified as delayed-fission γ-rays unique to the fissionable materials. A numerical model of the experimental setup is also proposed as part of this research. This model is based on the Monte Carlo radiation transport code MCNPX. The data from the experiment were used to validate the numerical models. Additionally, photonuclear data libraries were tested in the numerical model for consistency and accuracy. The numerical results showed a good agreement with the experimental data, specifically the comparison of ^{238}U. Discrepancies between the numerical results and experimental data of ^{232}Th were observed. A new photonuclear data library from TENDL/ACE was then implemented for ^{232}Th and the numerical results were improved. One of the main contributions of this work is the development of a reliable computational model that gives almost the same results that could

be performed on a physical experimentation as a less expensive option to examine the factors that could fall behind the spectroscopy measurements.

TABLE OF CONTENTS

LIST OF FIGURES

CHAPTER 1

INTRODUCTION

The sustainability of nuclear security enforcement both at borders and within states has become part of a global initiative to combat the unauthorized movement of nuclear materials outside of regulatory control. Considerable emphasis has been placed on the strengthening of border security capabilities through the development of new techniques to prevent, detect, and respond to acts of nuclear proliferation (*4*). Innovative techniques used to detect and identify the presence of special nuclear material (SNM) are of primary interest in the nuclear safeguards community. Although nuclear materials naturally emit neutrons and/ or γ-rays, these spontaneous emissions are typically detected as low intensity signals. It can also be assumed that the detection of such weak signals will be further limited by the presence of shielding to circumvent passive detection. Passive techniques for detecting shielded SNM rely on the detection of radiation emitted and on the detection of indirect radiation generated in the vicinity of the SNM, such as prompt γ-rays generated from thermal neutron capture (*5*). Although these techniques are fast and an equally important part of the border inspection effort, proper detection of concealed nuclear materials requires techniques that can unequivocally detect specific attributes of the nuclear materials (*6*).

Active inspection techniques using a particle beam as the interrogating radiation source for the detection and localization of nuclear materials has become of great interest

in nuclear security applications. These active techniques use an interrogating source of neutrons or high-energy γ-rays to stimulate nuclear reactions in the inspection object and then monitor the emitted secondary radiation for unique fissionable material signatures (*7*). A beam of high-energy γ-rays with energy greater than 6 MeV will cause SNM to fission. However, that beam will also cause other fissionable materials in the environment to fission, including natural uranium, so the emission of γ-rays resulting from interrogation by a high-energy γ-ray beam in itself is not a definitive indication of the presence of SNM (*8*). Therefore, a method that differentiates these "false" signals from the signal of the SNM should be proposed.

In photofission reactions, four types of radiation can be used as signature signals for material identification and quantification: prompt photons, prompt neutrons, delayed photons, and delayed neutrons. Although prompt signals are much stronger than the delayed signals, it is difficult to quantify them in practical measurements. The reason is that they tend to be buried by the much more intense probing radiation. Prompt γ-rays are emitted within 10^{-15} seconds as a result of energy redistribution accompanying fission. As the highly excited fission fragments de-excite, γ-rays are emitted up to a few microseconds after fission, as a result of isomeric transitions (*1*).

Delayed signals are emitted seconds or even minutes after the photon irradiation, thus making them much easier to be distinguished from the interrogating radiation. Delayed γ-rays have a wide range of half-lives ranging from fractions of a second to many years following induced fission. Approximately, 6 to 8 of these delayed γ-rays are emitted following each fission process. This is over 100 times more abundant than the yield of delayed neutrons. However, delayed neutron emissions are a direct indicator of nuclear

material (*9*).The number of delayed neutrons and γ-rays is proportional to the number of prompt neutrons emitted by a fissioning isotope (*10*). A delayed γ-ray energy spectrum is unique for each fissionable isotope. The spectra of delayed γ-rays are complex due to the contribution of γ-rays from many fission products. The relative amplitudes of certain lines vary significantly from one isotope to another which is a result of the difference in photofission yield distribution of the various isotopes.

Previous research has shown that delayed γ-ray spectra emitted by fission products can be measured in seconds or even minutes after the induced fission using high-purity germanium (HPGe) detectors (*11*). The time behavior of these fission products are dictated by the half-life of the fissioning nuclei. Thus, the time and energy characteristics observed in a measured γ-ray spectrum can be used to identify and quantify the fission products of nuclear materials. Since high-energy γ-rays are predominantly emitted from short-lived fission fragments, these γ-rays are indicative of the current amount of fissionable material in the sample (*7*). Using the knowledge on photofission yield distributions of various isotopes and the irradiation and count time intervals, the isotopic composition of the sample can then be deduced.

This thesis discusses the results obtained from high-energy photon interrogation of: depleted uranium (enriched to 0.2% ^{235}U), ^{239}Pu, and ^{232}Th. An active interrogation technique based on the delayed γ-rays following photon-induced fission events is evaluated. Predicted energy spectra of delayed γ-rays from photon-induced fission were conducted to incorporate a benchmark comparison to experimental data using the MCNPX 2.7.0 Monte Carlo radiation transport code. The photonuclear interaction capabilities of MCNPX were demonstrated using materials composed of ^{235}U, ^{238}U, ^{232}Th, and ^{239}Pu. Due

to the limited availability of photonuclear data in MCNPX, evaluated photonuclear data tables were acquired from two different sources and the validity of each source was investigated. The contents of this thesis will start by describing the physics of photofission and the method of delayed γ-ray detection, identification, and quantification. It will continue by describing experimental measurements of delayed γ-rays from nuclear material samples. A full description of the simulation methodology is then provided and the results are compared to the experimental measurements.

CHAPTER 2

METHODOLOGY

2.1 Nuclear Fission and Photofission

Nuclear fission represents a class of nuclear interactions in which the nucleus of an atom separates into two or more fission fragments. Fission can either be induced by a nuclear reaction or occur as a spontaneous process. For a nucleus to undergo fission in either process, the nuclear strong force must be exceeded by Coulomb repulsion between its protons. This separation of a nucleus into any possible combination of nucleons is governed by its binding energy and Coulomb forces. It can be determined which nuclei will fission by using the von Weizsacker semi-empirical mass formula based on the liquid drop model. The Weizsacker formula treats the nucleus as a collection of interacting particles and is written in terms of the total binding energy, given by

$$B({}^{A}_{Z}X) = a_v A - a_A A^{2/3} - \frac{3}{5}\frac{Z(Z-1)e^2}{4\pi\epsilon_0 r} - a_S\frac{(N-Z)^2}{A} + \delta \qquad (2\text{-}1)$$

where the volume term (a_V) indicates that the binding energy is approximately the sum of all the interactions between the nucleons, proportional to the total number of nucleons (A). The second term represents the surface effect and is a correction to the first term, because the nucleons on the nuclear surface are not completely surrounded by other nucleons. The third term represents the Coulomb repulsion between protons (*12*). For heavy nuclei, the nucleus will have preference for fewer protons than neutrons because of large Coulomb

repulsion energy. Because the Coulomb force is long range, the proton interacts electromagnetically with all the protons already in the nucleus. And because this repulsive energy increases with Z, nuclei with higher Z eventually become unstable. Figure 2-1 shows a plot of the known nuclides with neutron number N versus proton number Z. The line representing the stable nuclides is called the *line of stability*, indicating equal numbers of neutrons and protons. Nuclear binding energy is maximized for cases when N=Z (*13*). Although the line of stability represents the most attractive average internucleon nuclear force, the Coulomb force must also be considered. As the number of protons increase, the Coulomb repulsive force between the protons becomes stronger and reduces the binding energy. In the case of spontaneous fission, the semi-empirical mass formula reveals that fission occurs for nuclei with $Z^2/ A \geq 49$; however, such nuclei are rare and the decay rate is very low *(12, 14)*.

Fission may also be induced by a nuclear reaction in which a source of radiation imparts energy to the nucleus, initiating the fission process. Induced fission typically occurs through neutron absorption by a heavy nucleus which forms a highly excited compound nucleus that may quickly fission. Another primary form of radiation used to induce fission is high-energy γ-rays. The γ-ray excitation of a nucleus causing a deformation and eventually the fissioning of a nucleus is termed *photofission*. If the energy of the γ-ray lies within the giant dipole resonance (GDR), oscillatory motion is induced which deforms the nucleus. This deformation allows Coulomb repulsion to overcome the short-range strong force within the nucleus and scission occurs. Once scission occurs, the fission fragments are quickly accelerated apart (*13*). The fission fragments then emit prompt neutrons and γ-rays after about 10^{-20} seconds after fission. 10^{-17} seconds after

fission, prompt γ-rays are emitted from the fission fragments. 10^{-2} seconds after fission, the fission fragments then undergo β-decay and emit delayed neutrons and delayed γ-rays.

Photonuclear absorption consists of nuclear interactions initiated by photons. This threshold process lies between 5-13 MeV and the cross-section increases rapidly above this threshold energy to form the GDR. The nature of photonuclear interactions and the resulting distributions from fission fragments is governed by this maxima in the photon absorption cross-section of nuclei (*15*). The GDR is characterized by the collective oscillation of neutrons and protons in nuclei which can be excited by an electromagnetic field, leading to a resonance response of nuclei where neutron and proton densities are shifted and a change in the potential energy of the system occurs (*16*).

Understanding the mass and charge distributions in photon-induced fission of actinides provides information pertaining to the energy characteristics of the fission yields. The amount of excitation energy required to make fission possible can be estimated from the height of the nuclear potential barriers and the disassociation energy for the particular mode of fission (*1*). The photofission process is a barrier-penetration process similar to neutron-induced fission in isotopes with even atomic weight. For example, the photofission cross-section of ^{238}U in Figure 2-2 is shown exhibiting a sharp increase near 1 MeV and around 6 MeV. It is important to note this behavior occurs at 6.5 MeV, the fission excitation energy for ^{238}U. Observation of these trends indicate the role of excitation energy on fission yields of an isotope. Being that the distribution of fission fragments are responsible for the delayed emissions of γ-rays, the resulting energy spectra is unique to the fissioning isotope.

2.2 Physics of HPGe Detectors

High-purity germanium (HPGe) detectors comprise a class of solid-state spectroscopy systems commonly utilized for their superior energy resolution capabilities. Unlike that of scintillation detectors, the charge produced by photon interactions is collected directly in solid-state detectors. The energy of electrons inside a pure material, such as in high-purity germanium, is confined to an allowed energy range within a solid. These ranges describe allowed energy states for electrons that are nearly continuous over certain ranges, called energy bands. Between these energy bands exists forbidden energy gaps in which the electrons cannot occupy, called energy band gaps (*12*). In semiconductor detectors, there are two energy bands of interest: the valence band and the conduction band. The valence band corresponds to outer-shell electrons that are bound to specific lattice sites within a crystal, and the conduction band represents electrons that are free to migrate through the crystal. In semiconductors, the gap between the valence and conduction bands is small enough that if an electron gains an energy greater than or equal to this band gap energy, it will move into the conduction band, making itself available to electrical conductivity. Promoting an electron into the conduction band in turn leaves a hole in the valence band, thus creating an electron-hole pair (Gamma-ray Spectroscopy.pdf). These liberated electrons and holes move freely and a biased voltage is applied across electrodes in the semiconducting material, creating an electric field which sweeps the charge carriers to collecting electrodes. As illustrated in Figure 2-3, a preamplifier then converts the collected charge into a voltage pulse proportional to the energy deposited into the detector.

Three different interactions describe how γ-rays will interact within a medium: the photoelectric absorption, Compton scattering, and pair production. In all three of these

processes, the γ-ray transfers either all or part of its energy into the medium with which it interacts. In photoelectric absorption, a photon interacts with a bound electron and one of the atomic electrons is ejected as a free electron, called a photoelectron (*17*). As shown in Figure 2-4, this process results in an ejected electron in conjunction with complete absorption of the incoming photon or an ejected characteristic X-ray. In a γ-ray pulse height spectrum, the ejected electron is recorded at the energy of the incident photon. When a γ-ray interacts with lead shielding around a detector, lead X-rays are produced and are recorded at about 72 keV.

In a Compton scattering event, as depicted in Figure 2-5, an incoming photon collides with a free electron, transferring part of its energy to the electron. The energy of the scattered photon and the recoil electron is dictated by the scattering angle of the photon. The kinetic energy of the scattered electron as a function of the scattering angle and energy of the incident photon is given by

$$E_e = \frac{(1-cos\theta)E_\gamma/mc^2}{1+(1-cos\theta)E_\gamma/mc^2}E_\gamma \qquad (2\text{-}2)$$

where θ is the scattering angle of the photon and E_γ is the energy of the incident photon. The maximum energy of the electron is obtained when θ = π, and the minimum energy when θ = 0. Compton scattering interactions create electrons that are lower in energy about this minimum-maximum range, forming what is called the Compton Continuum in a γ-ray pulse height spectrum.

Pair production occurs when a γ-ray is absorbed by a nucleus and an electron-positron pair is created. This process is illustrated in Figure 2-6. The photon generates this electron-positron pair in the Coulomb field of the nucleus and has a photon energy threshold that is equal to the rest mass energies of two electrons, $2m_ec^2$ = 1.022 MeV (*14*).

The mutual electrical attraction of the electron-positron pair cause the particles to undergo *pair annihilation* during which the particle and its antiparticle orbit around their common center of mass and annihilate each other. Upon annihilation, and due to conservation of energy of the system, two 0.511 MeV photons are emitted. As shown in Figure 2-7, in a γ-ray pulse height spectrum, absorption of both annihilation photons produces a peak called the *single escape peak*, recorded at exactly 0.511 MeV less than the original γ-ray energy. When both annihilation photons are not absorbed, a separate peak called the *double escape peak*, is recorded at exactly 1.022 MeV less than the original γ-ray energy. Contrary to photon absorption, incident photons with significant enough energy are capable of passing directly through the active region of the detector, depositing only a fraction of their energy.

HPGe detectors are the preferred choice for the analysis of complex γ-ray spectra involving many energy peaks in γ-ray spectroscopy analysis (*18*). These solid-state detectors are commonly made in two configurations: planar and coaxial. These two configurations describe the geometry of the semiconductor material with respect to electrical contact surfaces within the detector volume. These coaxial detectors are produced as either true coaxial or closed-end coaxial. The true coaxial configuration has one electrode fabricated at the outer cylindrical surface of a long cylindrical germanium crystal and a second cylindrical contact within the inner cylindrical surface of the crystal. A closed-ended coaxial configuration has a similar construction to that of the true coaxial but with only part of the central core removed and the outer electrode extended over the flat end of the cylindrical crystal. The closed-ended configuration provides a planar front surface which serves as an entrance window for weakly penetrating radiation fields. The

useful energy range of the coaxial detector is 40 keV to more than 10 MeV but comes at the cost of low detection efficiencies in high count rate environments.

2.3 Overview of Active Interrogation Using Photofission

According to the Atomic Energy Act of 1954, special nuclear materials are defined as plutonium, ^{233}U, or uranium enriched in the isotopes ^{233}U or ^{235}U (*19*). For example, when bombarded with neutrons, ^{232}Th becomes ^{233}Th, which eventually decays into ^{233}U, a fissionable material that can be used as nuclear fuel. In this regard, it is similar to ^{238}U which by the same process transmutes to ^{239}Pu. The nuclear regulatory commission (NRC) has classified these materials as those which are capable of releasing substantial quantities of atomic energy and carry a potential of being used in a nuclear explosive device. Therefore, nuclear materials consisting of ^{232}U, ^{235}U, ^{238}U, and ^{239}Pu are of particular interest to the nuclear safeguards community.

The detection and identification of delayed emissions between intense Bremsstrahlung pulses have been largely investigated in the past *(5, 13, 20-24)*. The need for innovative active interrogation techniques brings with it the challenge of identifying unique fission events while in the presence of a high-energy interrogation field. Currently, the detection and measurement of delayed emissions require discrimination between fission radiation and the interrogating source. Active interrogation with high-energy photons currently depends on the β-delayed neutrons following fission to provide a unique signature for fissile material (*20*). However, the relatively low yield of delayed neutrons (~ 0.01 to 0.02 neutrons per fission) and the effect of hydrogenous shielding for neutron attenuation causes low detection sensitivities. On the other hand, prompt γ-rays from photofission are very difficult to measure because of the extremely high background signal

of γ-rays from the interrogating source (*1*). However, the intensity of delayed γ-ray signatures, at energies above 3 MeV, are nearly 10 times more intense and undergo 10-100 times less attenuation than that of delayed neutrons (*21*). The total energy carried out by delayed γ-rays per fission is approximately 6-8 MeV, making the average energy of delayed γ-rays about 1 MeV (*21*).

Acquisition of time and energy information from induced photofission reactions provide a key tool in the identification of the fission products. Photons with energies above 6 MeV can be used to induce fission on actinides (*22*). Previous research has shown that a unique delayed gamma ray energy spectrum exists for each fissionable isotope based upon their fission product distributions *(6, 16, 23-25)*. E. Norman et al. successfully detected β-delayed γ-rays and showed how the energy spectra and time dependency from these emissions provide unique signatures for ^{235}U and ^{239}Pu (*20*).

In addition, β-delayed γ-rays have also been measured as a signature signal for the detection of SNM by researchers at Idaho National Laboratory (IAC). Work by E. Reedy and A. Hunt shows that γ-rays detected in the energy region above 3 MeV and beyond 35 ms are β-delayed γ-rays from short-lived fission fragments *(7, 13)*. Their work used the isotopic mass and elemental fission fragment distributions from actinide nuclei ^{238}U, ^{239}Pu, and ^{232}Th using bremsstrahlung with a 22 MeV endpoint energy to identify these delayed signatures.

Delayed signals expected in photofission events can be predicted using the fission fragment distributions of SNM. The distribution of fission products directly depends on the nature of actinides. The differences between their distributions can be measured by the detection of delayed γ-rays emitted by the fission products (*26*). Spectrometric techniques

used on various fission products of nuclear materials from bremsstrahlung are seen in the literature. H. Naik et al. showed that around the GDR region, bremsstrahlung- and neutron-induced fissions of ^{232}Th and ^{238}U exhibit significant fission and reaction cross-sections (*25*). The investigation showed that with excitation energy, an increase yield of symmetric products and the decrease of the peak to valley (P/V) ratio in the ^{238}U(γ,f) reaction is similar to the ^{238}U(n,f) reaction.

For the photofission of ^{238}U, B. Ishkhanov et al. investigated the independent and accumulated yields of separate photofission products following the emission of delayed neutrons using bremsstrahlung with 19.5, 29.1, 48.3, and 67.7 MeV endpoint energies (*27*). This research shows that the total energy that is liberated in the process of nuclei fission is distributed between the kinetic energy of fragments and their inner excitation energy which plays a crucial role in the mass distributions of photofission fragments. In addition, the yield of fission products around mass numbers 133-135 is more pronounced compared to mass numbers 143-145, in both neutron and bremsstrahlung fission of uranium isotopes and heavier actinides (*28*). F. Carell et al. demonstrated the capability to experimentally differentiate between actinides ^{235}U, ^{238}U, and ^{239}Pu using ratios between two γ peaks emitted in the same energy range of the spectrum (*26*).

The choice of photon interrogation energies used in the literature discussed above is based around the fission excitation energy of a particular nucleus. Because these photonuclear interactions are threshold interactions, the selected incident beam energies used never fall below certain energies depending on the target nuclei. Figure 2-8 compares the photofission cross-sections for ^{232}Th, ^{238}U, and ^{239}Th. It is important to point out here that the cross-sections are energy dependent and well above the photofission barrier they

are nearly the same. However, their characteristics at lower energies make it possible to distinguish between the various fissionable isotopes (*1*). Photofission in the case of actinides has a giant dipole resonance centered around 10-15 MeV and below about 5 MeV, these cross-sections significantly drop with decreasing incident photon energy. High-energy photons above 20 MeV can remain effective inducers of fission despite the fact that they exceed the energy of the giant dipole resonance region (*29*).

When compared to neutron-induced fission, less experimental effort has been directed at measuring delayed photofission products, but the use of reaction-channels provide a means for approximating the emissions (*29*). Monte Carlo radiation transport simulations of neutron-induced and photon-induced photonuclear events using MCNPX have been well studied in the past *(15, 23, 30-35)*. Correlations between neutron-induced fission and photofission of a nucleus introduce approximations about excited nuclei prior to scission which allows for gaps in the available experimental data to be bridged for calculations and modeling purposes (*36*). Simulating photonuclear physics using Monte Carlo radiation transport codes have primarily focused on prompt- and delayed-neutron events and in effect have required photonuclear data for neutron-induced events. Calculations in MCNPX involving energy discrimination and time behavior characteristics of delayed γ-ray from photon-induced interactions are not fully supported in the literature. However, modeling of the photofission yield through known neutron-induced fission yield was carried out by E. Reedy et al. (*13*) who used fission fragment distributions from ENDF/B-VII.0 and discrete line information from ENSDF to simulate the energy spectra of ^{238}U and ^{232}Th.

Applications in MCNPX involving production intensities of delayed γ-rays produced from neutron-induced fission of fissile materials was performed by J. Durkee et al. along with D. Beddingfield and F. Cecil *(23, 33)*. Durkee, Beddingfield, and Cecil reported on calculated pulse-height spectra for ^{235}U and ^{239}Pu and compared with experimental data in an energy region from 0 MeV to 1.5 MeV. T. Wilcox et al. integrated the Cascading γ-ray and Multiplicity (CGM) V3.4 code within MCNPX to compensate for the lack of experimentally unmeasured quantities which are not represented by the ACE data libraries in MCNPX (*37*). While this implementation is capable of producing delayed γ-ray multiplicities per interaction, minor improvements to resolve the individual energy peaks were observed.

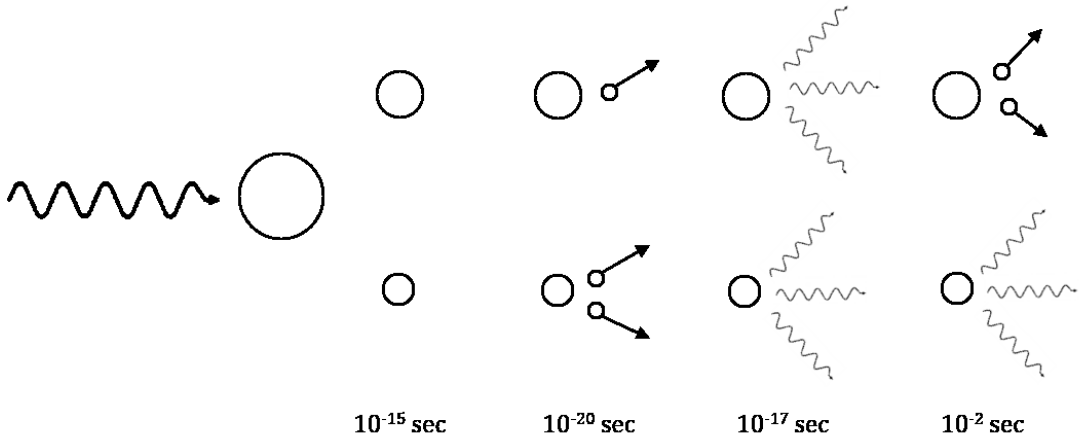

Figure 2-1. Schematic of the photofission process. 10^{-15} seconds after irradiation, the nucleus splits into two separate fission fragments. 10^{-20} seconds after irradiation, 2-3 prompt neutrons are emitted. 10^{-17} seconds after irradiation, 6-8 prompt γ-rays are emitted. 10^{-2} seconds after irradiation, 6-8 delayed γ-rays are emitted (*1*).

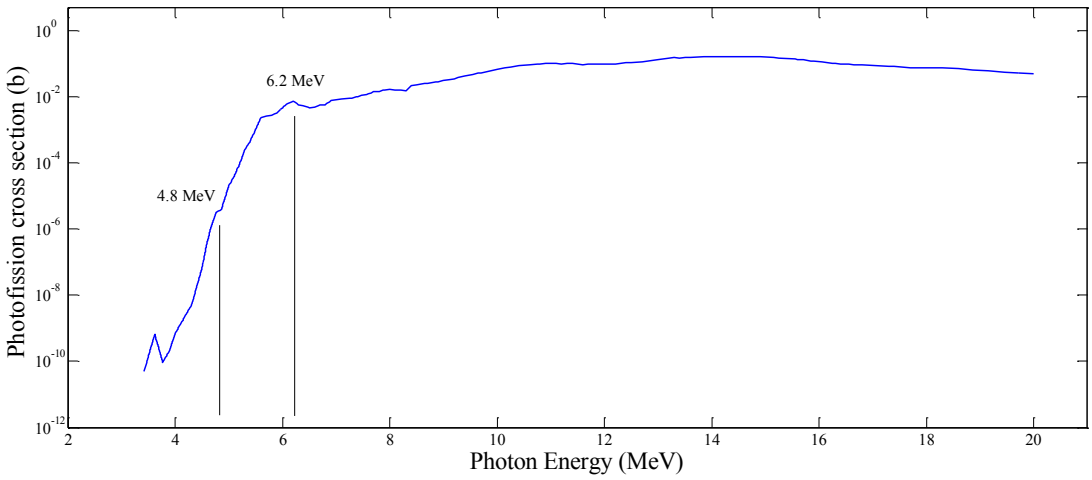

Figure 2-2. Photofission cross-section for ^{238}U between 0 to 25 MeV (*2*). Energy abscissa at 6.2 MeV and 4.8 MeV indicate estimated fission excitation energy and binding energy for ^{238}U nucleus, respectively. These sudden peaks in the ^{238}U cross-section can be used to indicate the threshold interaction energies. This plot illustrates a high-probability region of interest to applications of photon-induced reactions well above the photofission barrier up to 20 MeV.

Figure 2-3. Schematic of semiconductor detector components used for γ-ray spectroscopy. Electron-hole pairs are created following excitation due to incoming γ-rays. High-purity germanium semiconductor detectors must be housed in a vacuum-tight cryostat and cooled to liquid nitrogen temperatures (77 K) to inhibit thermal conductivity between the detector crystal and its surrounding environment. In most cases, the detector crystal and preamplifier are unified, whereas the amplifier and MCA are separate units.

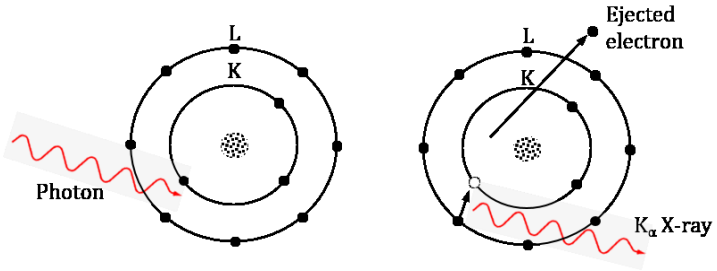

Figure 2-4. Photoelectric interaction of a photon ejecting a bound electron and a photon ejecting a characteristic X-ray.

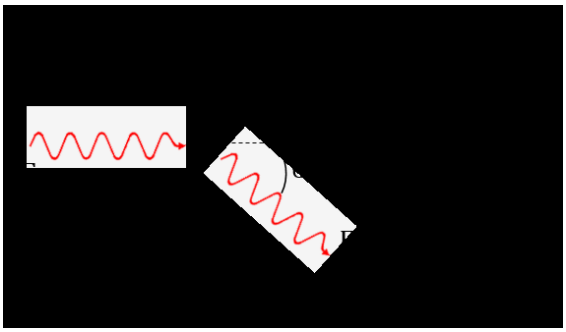

Figure 2-5. Compton scattering of a photon by an electron at rest.

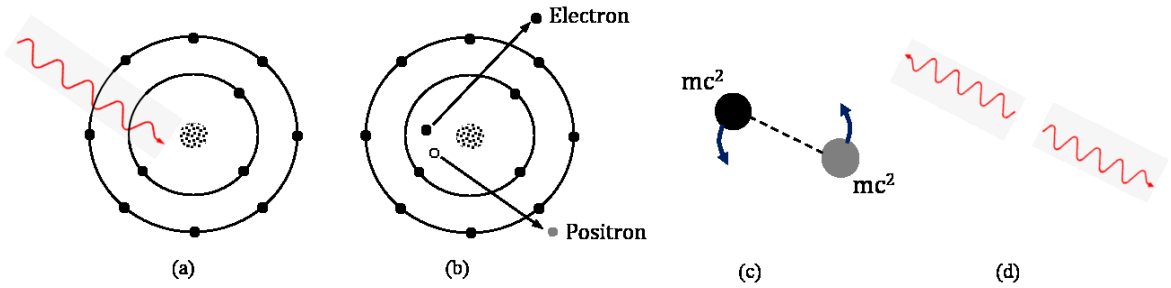

Figure 2-6. Pair production. (a) A photon interacts with the electrons of a nucleus. (b) An electron-positron pair is created. (c) The electron-positron pair annihilate each other. (d) Two annihilation photons are produced, each at an energy equal to the rest mass of the electron and positron $mc^2 = 0.511$ MeV.

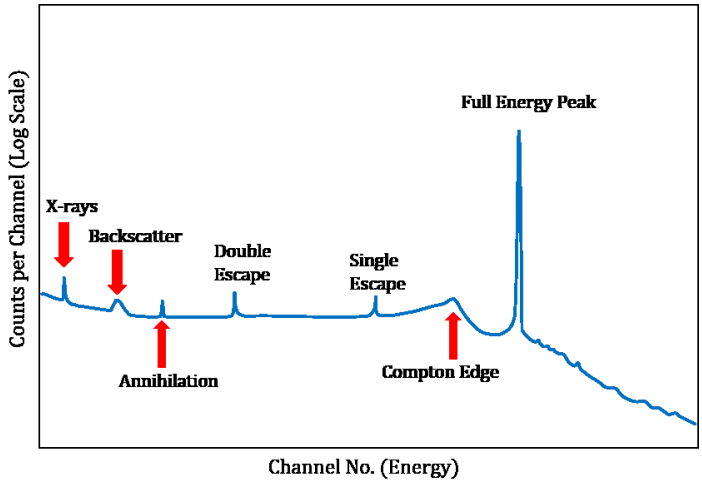

Figure 2-7. Common pulse features that characterize a γ-ray energy spectrum. The X-ray peak is caused by γ-rays interacting with lead shielding via photoelectric interaction. The backscatter peak is caused from scattered photons escaping a detector and the Compton edge from scattered electrons escaping at a maximum energy, via Compton scattering. The single and double escape peaks are caused by annihilation photons created through electron-positron pair production. The annihilation peak is caused by pair production occurring outside a detector when only a single annihilation photon is recorded.

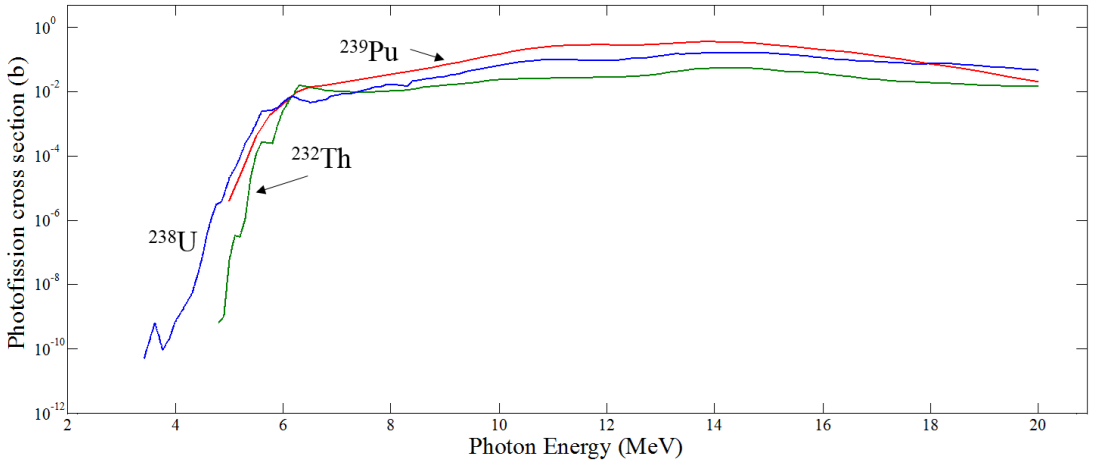

Figure 2-8. Photofission cross-section for ^{232}Th, ^{238}U, and ^{239}Pu from about 3 to 20 MeV as a function of photon energy (*2*). These sudden peaks in each cross-section indicate the photofission barriers (over 6 MeV). This plot illustrates the region of interest for applications of photon-induced reactions well above the photofission barrier up to 20 MeV. At low energies, the cross-section behavior of these nuclear materials exhibit unique characteristics. From this plot, it can be deduced that interrogation of these nuclei with photons above 6 MeV will cause each to undergo fission.

CHAPTER 3

EXPERIMENTAL MEASUREMENTS OF DELAYED γ-RAYS

3.1 Experimental Setup

3.1.1 Photon Interrogation

An intense, pulsed bremsstrahlung photon beam was used for inducing photofission in fissionable materials. The 25 MeV pulsed linear accelerator was operated at 22 MeV, carrying 150 nC of charge and with a pulse rate of 15 Hz. The accelerator pulse width was 4 μs, resulting in data acquisition between pulses for approximately 67 ms. The bremsstrahlung photon beam was produced by an electron beam incident on a 4.2 g/cm^2 tungsten radiator and was passed through a series of lead collimators contained within a 1.8 m thick concrete wall, separating the accelerator hall and experimental cell. The beam collimation consisted of two lead collimators, each 15.2 cm in length. The first collimator was 1.27 cm in diameter and placed 61 cm from the tungsten radiator on the beam hall side of the concrete wall. The second collimator was 3.81 cm in diameter, 1.79 m from the tungsten radiator on the experimental side of the concrete wall. The resultant beam at the target location had an approximate diameter of 7.5 cm, 4.0 m from the tungsten radiator. Figure 3-1 shows a schematic of the experimental setup.

Two 20% relative efficient Canberra GC2020 n-type coaxial high-purity germanium (HPGe) detectors were positioned on each side of the bremsstrahlung beam. The entrance window of each detector was aligned perpendicular to the beam line and the

body of each detector was shielded with 10.16 cm of lead, followed by 10.16 cm of borated polyethylene. An additional 5.08 cm of lead shielding was added to the side of each detector that faced the beam side of the experimental cell. The detection region of each detector was collimated with lead bricks to produce a 5.08 cm opening and capped with a 2.54 cm lead brick to reduce detector dead time due to high count rate. The shielded assembly contained within the experimental hall is shown in Figure 3-1. The detectors and front-end electronics are positioned in shielding cavities built with lead and borated polyethylene.

Three targets were used during the extent of this experiment: a 18.9 g/cm^2 ^{238}U plate; a 28.8 g/cm^2 lead brick; a 1.0 gram, 19.8 g/cm^2, 60μCi ^{239}Pu sample; and four 6.0 g/cm^2 ^{232}Th cylinders. The targets were positioned directly in the beams path, and approximately 20.0 cm from each detector face. The distance from the target location to the second collimator was 15.5 cm, about 2.0 m from the tungsten radiator.

3.1.2 Data Acquisition

Three separate signal processing units were used to acquire data: a FAST ComTec list mode system, a Canberra LYNX multichannel analyzer (MCA), and a customized system based on a National Instruments high-speed digitizer. The FAST ComTec list-mode system is an analog data acquisition system which records both energy and time information for each individual γ-ray event.

The Canberra LYNX MCA was operated by the Canberra Genie 2000 software running on a host PC. The data acquisition was set in the 'coincidence mode', which indicates data acquisition upon trigger of the external GATE signal. In the following experiments, an arbitrary-function generator (Agilent AFG3021C) was used to produce the

GATE signal, triggered by each accelerator pulse and staying active for 20 ms. This indicates that the LYNX MCA was disabled for 20 ms after each accelerator pulse. Data collection was then initiated following the start of the next accelerator pulse.

The digitizer used was a PXIe-5122 module from National Instruments. The sampling rate used during the experiment was 5 Msps. The resolution of the digitizer is 14 bit. A LabVIEW program was developed to stream digitized data onto a hard drive array with full speed at 10 Mb/s. One can set operating parameters for the digitizer and control the digitization/recording process using this program. The digitizer is triggered by an external trigger generated by each accelerator pulse. The length of each data acquisition cycle was programmed to account for the entire time duration between adjacent accelerator pulses. Signal processing for the digitized data was performed offline in Matlab® based on trapezoidal filters for optimal balance between throughput rate and resolution and real-time processing. To implement pile-up rejection, two separate signal paths with different shaping parameters were designed. The slow channel was used for accurate energy measurement, while the fast channel was utilized to measure the arrival time for each event. The algorithm was designed such that when a pile-up was detected, the affected pulses were disregarded. This assured a clean spectrum even in ultra-high count rate scenarios (>105 cps).

3.2 Irradiation Measurements

Emissions from photofission have been measured for the four actinide nuclei ^{238}U, ^{239}Pu, and ^{232}Th. Fission product γ-rays were measured between beam pulses after the irradiation of depleted uranium (0.2% enriched ^{235}U), ^{239}Pu, and ^{232}Th. The depleted uranium (DU) was irradiated for two hours using a bremsstrahlung beam pulse of 150nC

at 15Hz (~10^5 pulse cycles). Data acquisition was performed using the Canberra LYNX MCA on HPGe 1 and the ComTec list-mode system on HPGe 2. The gate signal of the MCA was set to 20 ms. The first 10 ms were omitted while counting the DU. The DU samples were irradiated a second time for two hours but the National Instruments digitizer was used in place of the LYNX MCA.

The ^{239}Pu sample was irradiated for 100 minutes using a bremsstrahlung beam pulse of 150nC at 15Hz (~10^5 pulse cycles). Data acquisition was made using the Canberra LYNX MCA on HPGe 1 and the ComTec list-mode system on HPGe 2. Again, the gate signal of the MCA was set to 20 ms. The first 20 ms were omitted while counting the DU. In a second scenario, the ^{239}Pu was irradiated for four hours using a bremsstrahlung beam pulse of 150nC at 15Hz (~10^5 pulse cycles). Data acquisition was made using the Canberra LYNX MCA on HPGe 1 and the ComTec list-mode system on HPGe 2. The first 20 ms were omitted while counting the ^{239}Pu.

The ^{232}Th cylinders were irradiated for three hours using a bremsstrahlung beam pulse of 150nC at 15Hz (~10^5 pulse cycles). Data acquisition was made using the National Instruments digitizer on HPGe 1 and the ComTec list-mode system on HPGe 2. In addition, a 28.8 g/cm^2 lead brick was irradiated for 10 minutes using a bremsstrahlung beam pulse of 150nC at 15Hz (~10^5 pulse cycles). Data acquisition was made using the National Instruments digitizer on HPGe 1 and the ComTec list-mode system on HPGe 2.

Full energy peaks from fission products were observed and identified in these spectra. Figure 3-2 shows the γ-ray energy spectra of the 18.9 g/cm^2 ^{238}U plate, the 28.8 g/cm^2 lead brick, the 1.0 gram, 19.8 g/cm^2, 60μCi ^{239}Pu sample and the four 6.0 g/cm^2 ^{232}Th cylinders. While spectra from ^{238}U, ^{239}Pu, and ^{232}Th targets show elevated yields above 3

MeV, the spectrum produced from the lead target shows a sharp cut off in its spectrum above this energy. Although delayed γ-rays can also be produced in the lead sample due to the production neutron capture γ-rays, these reactions are much shorter lived than fission γ-rays (*32*). Due to the γ-ray energy emissions from natural occurring background radiation never exceeding 2.6 MeV, γ-rays detected above this energy level can be attributed the irradiated materials.

Figure 3-3 illustrates the LINAC beam pulse structure used throughout the measurements. The presence of detectable γ-rays from the presence of short-lived fission fragments exist approximately 10 ms following the beam pulse. These fission products being produced during each LINAC pulse have relatively short half-lives and quickly decay away. In order to capture short-lived isotopes and increase the sensitivity of the measurement, it is preferred that spectrometry measurements be performed in between LINAC pulses. Observations of the output signal from the HPGe detector pre-amplifier after each LINAC pulse were made. Because of the huge energy deposition during each pulse, the detector and front-end electronics are saturated for a relatively long time period (~tens of ms). After this, the baseline slowly returns to zero, as shown in Figure 3-3. Traditional shaping methods cannot handle this behavior very well, so the measurements have to be gated. In the following measurements, the LINAC was running at 20 Hz, i.e., the time interval between two adjacent pulses is 50 ms. Following each pulse, the MCA waits for 20 ms before starting processing incoming signal. The counting continues for 20 ms before the MCA is disabled right before the next pulse hits.

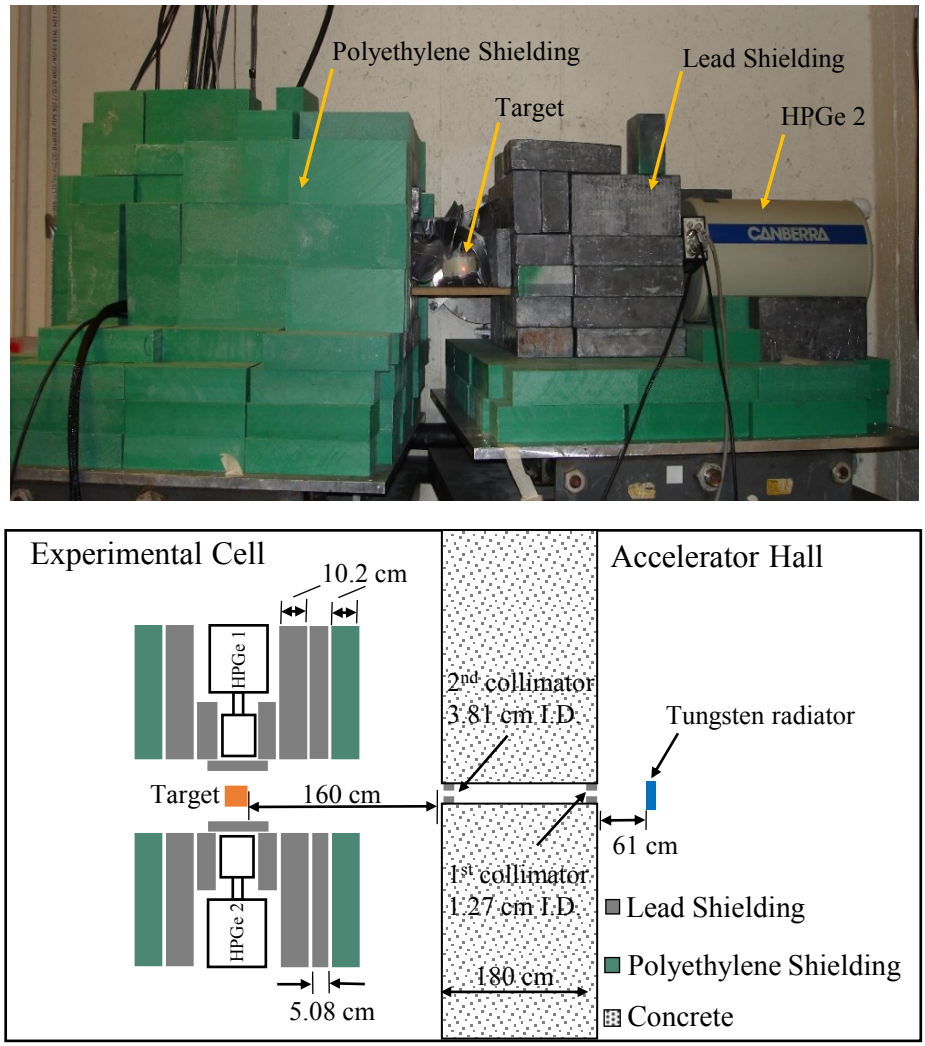

Figure 3-1. Picture and drawing of the experimental setup used to measure γ-ray spectra from photofission. Two shielded Canberra GC2020 n-type detectors were placed perpendicular to the bremsstrahlung beam path. The resultant beam at the target location had an approximate diameter of 7.5 cm, 4.0 m from the tungsten radiator.

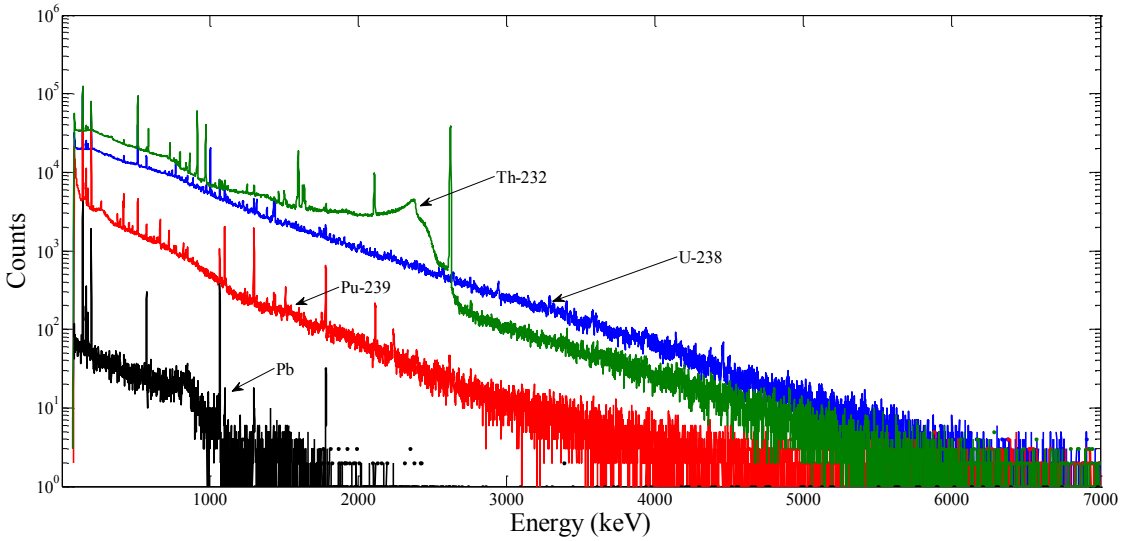

Figure 3-2. Energy spectra of 18.9 g/cm^2 ^{238}U plate; a 28.8 g/cm^2 lead brick; 1.0 gram, 19.8 g/cm^2, 60μCi ^{239}Pu sample; and four 6.0 g/cm^2 ^{232}Th cylinders measured with a Fast ComTec list mode system. Spectra were produced using a 22 MeV bremsstrahlung beam pulse of 150nC at 15Hz. Data from the first 10 ms following each LINAC pulse were removed.

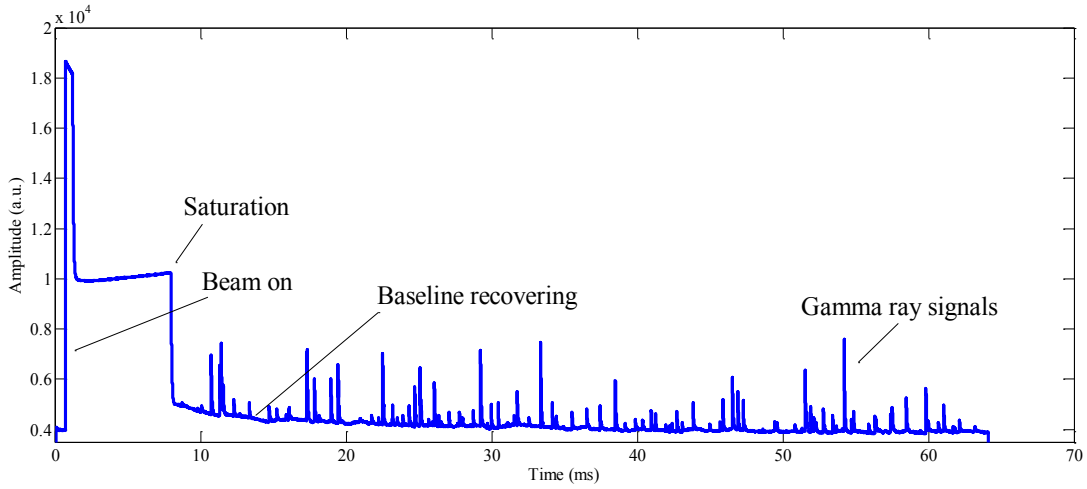

Figure 3-3. LINAC beam profile measured on the Genie2000 MCA software. As the LINAC triggers, detectors become fully saturated while exposed to intense field. The baseline of the output single slowly returns to normal after each LINAC pulse. After each pulse, the MCA waits before starting processing of the incoming signal. The counting continues for a period before the MCA is disabled and the LINAC is again triggered. It can be observed in this case that the detector output is saturated for roughly 10 ms in this example.

CHAPTER 4

MONTE CARLO MODELING OF THE EXPERIMENT

4.1 Monte Carlo Method

The Monte Carlo method is a powerful numerical method used for solving particle transport problems. This method provides a numerical solution to a macroscopic system that makes an attempt to model macroscopic interactions found in nature. The solution to this method is determined by simulating individual particles and recording aspects of their behavior by satisfying the conditions of a transport problem. The linear time-independent mono-energetic Boltzmann transport equation is given by

$$\boldsymbol{\Omega} \cdot \nabla \Psi(\boldsymbol{r}, \boldsymbol{\Omega}) + \sigma(\boldsymbol{r}) \Psi(\boldsymbol{r}, \boldsymbol{\Omega}) = \int d\Omega' \, \sigma_s(\boldsymbol{r}, \boldsymbol{\Omega} \cdot \boldsymbol{\Omega}') \Psi(\boldsymbol{r}, \boldsymbol{\Omega}') + s(\boldsymbol{r}, \boldsymbol{\Omega}) \qquad (4\text{-}1)$$

where $\Psi(\boldsymbol{r}, \boldsymbol{\Omega})$ is the particle flux in terms of position **r**, and the particle direction of travel **Ω**. $\sigma(\boldsymbol{r})$ and $\sigma_s(\boldsymbol{r}, \boldsymbol{\Omega} \cdot \boldsymbol{\Omega}')$ are the macroscopic total and differential scattering cross-sections, respectively, and $s(\boldsymbol{r}, \boldsymbol{\Omega})$ is the external source term (*38*). The Boltzmann transport equation describes the transport of neutral particles from one collision with an atom to another. This equation accounts for contributions from radiation in a given increment of space, energy, direction, and time. Unlike deterministic methods of transport modeling, which solve the transport equation for average particle behavior, Monte Carlo methods do not explicitly solve the transport equation. Instead, individual particles are simulated, tracked, and some aspects of their average behavior are scored. The solution to the Boltzmann transport equation yields the expected behavior of a large number of

particle's. In the Monte Carlo method, each particle's behavior is then tallied, or the frequency for the particular event is recorded (*31*). In the Monte Carlo method, a stochastic model is constructed in which the expected value of a certain random variable is equivalent to the value of a physical quantity to be determined. This expected value is then estimated by the average of several independent samples representing the random variable (*35*). The probability distributions governing these events are then statistically sampled to describe the total phenomenon, or the physics of a given system. Monte Carlo methods use Markov processes to simulate such physical phenomena. Sampling of variables is done by generating random number sequences to sample probability distributions related to the system being simulated (*39*).

A probability density function (PDF) is a complete probability model of a continuous random variable. The PDF is the most useful probability model in that it provides a good indication of the likely values of observations. Another reason is that it plays a key role in calculating the expected value of a random variable (*40*). The importance of this function is its use in particle transport simulation in which the continuous-energy Monte Carlo utilizes PDFs which closely model the physics of particle interactions. Particle energy is a continuous variable, and a separate PDF is used for each type of particle interaction (*31*).

In a Monte Carlo calculation, a source particle is introduced with coordinates which may be sampled randomly according to PDFs representing the spatial, directional, and energy distributions of source particles in the specific physical problem considered. Probability distributions are randomly sampled using transport data to determine the outcome at each step of a particle's life (*41*). In the transport portion of the analysis, the

distance to the particle's next collision is sampled randomly from the PDF which describes the random-walk of particles in a given medium. Geometric information describing material and region boundaries, usually in the form of first or second degree surface equations, is then analyzed to determine whether the sampled distance to collision is less than the distance to a boundary.

The Monte Carlo simulation of a given experimental arrangement consists of the numerical generation of random histories. To simulate these histories, we need to model the interaction using a set of differential cross-sections for the specific interaction. The differential cross-sections determine the probability distribution functions of the random variables that characterize a track. These tracks include the mean free path between successive interactions, the interaction type, and the energy loss and angular deflection of that event. Once the PDFs are known, random histories can be generated by using appropriate sampling methods. If a large number of these histories can be generated, useful information on the transport process may be obtained by averaging over the simulated histories (*34*).

The capability of MCNPX to associate delayed γ-rays through line emission with their emitting radionuclide has been implemented (*42*). In the same respect as those methods just described, the creation of delayed γ-rays in MCNPX is done by randomly sampling probability distributions to determine their emission energy, the delay time following fission, and direction (*43*). Durkee et al. provide a full account of the statistical distribution theory derivations for each source formulation of the physical multigroup sampling methods (*43*). The derivation of the multigroup sampling method used in MCNPX is complimented by the theory and also code development for line sampling.

4.2 MCNPX Model Using 4-π Detection Geometry

Simulations were conducted in MCNPX to provide a benchmark comparison with experimental measurements of β-delayed γ-rays. Figure 4-1 illustrates the ideal 4-π detection geometry used in this simulation model. In this simplified model, three separate spheres centered about a xyz plane were used to define the problems geometry using the SO surface-type mnemonic within each surface card. Specification of surface parameters was completed by supplying the appropriate coefficients needed to satisfy the surface equation for a sphere. For example, a sphere of radius 10.0 cm centered at the origin (0,0,0) can be specified by entering SO 10 on a given surface card. Using this mnemonic, the first sphere was defined as the smallest of the three and contained the target material. Encompassing the target material region, two spheres with radii differing by only 1.0 cm were defined. The volume between these spheres was used as the detection region for this simplified approach. Finally, a fourth sphere was defined to set a boundary region containing all three smaller spheres.

Source specification was done using the general source SDEF card. An example of the general source definition used for this simulation is characterized by

POS = -10 0 0 VEC = 1 0 0 DIR = D1 PAR =2 ERG = 22 TME = 0

This source card allows the user to define a number of source parameters using any of its 22 available keyword variables. Setting the source variable PAR equal to 2 or P specifies photons as the source particle type. The energy of the photon point source was done by using the ERG variable and setting its value equal to 22. The location of this source was defined by assigning xyz coordinates to the POS variable. The source position was set on

the inner surface of the smaller detector sphere and directed inward toward the target material. The time behavior was defined by the TME keyword and set equal to 0.

The direction of the photon source was indicated by assigning a normal reference vector (1,0,0) to the variable VEC. The cosine of the VEC polar angle was controlled by setting the DIR equal to a distribution of another variable (D1). The parameters of this distribution were indicated on the source information (SIn) card whose nth parameter represents the corresponding distribution number. For this model, the SIn card was defined with the distribution numbers 0.89 and 1, indicating a histogram whose distribution contains cosine bin limits between 0.89 and 1. The values 0 and 1 were assigned to the source probability card (SPn), indicating the probability of its assigned distribution as either having a zero probability or being 100 percent probable. The target materials were defined using the material card (Mn) and concentrations were described in terms of weight ratios, denoted by a minus sign (-). Each material density was defined in terms of mass density (g/cm^3).

4.2.1 Photonuclear Physics

In order to simulate photonuclear interactions using MCNPX, the software's photonuclear physics option must first be invoked using the PHYS: P card. Photonuclear interactions used as the source of particles for each simulation were the primary mechanism of the photonuclear physics option used throughout this study. Indication of the symbol P on the MODE card (MODE P) was used to designate photons as the particle type to be transported in MCNPX. To enable the production of photons and neutrons from photofission reactions, the ispn entry of the PHYS: P card has to be changed from the default value (ispn=0) to enable photonuclear collision sampling. Furthermore, the fism entry of the PHYS: P card should be set to 1 to ensure that photofission secondaries are

sampled only when a photofission event occurs if the analog production of fission neutrons and γ-rays is desired. This is different from the default scenario (fism=0), where high-energy photons can produce secondary particles via a photonuclear interaction that is not necessarily from the same reaction. The energies and directions of the secondary particles are averaged over all possible photonuclear interactions which includes photofission. This default setting is only correct on average over a large number of interactions, thus its use is not suitable for applications where detail of secondaries production is important, for example, coincidence counting of photofission particles.

The capability to include photonuclear physics in MCNPX simulations via tabular data sampling was introduced but is limited by the availability of the data (*44*). Data tables exist for ten classes of data in MCNP: continuous-energy neutron, discrete-reaction neutron, continuous-energy photoatomic interaction, continuous-energy electron interaction, continuous-energy photonuclear interaction, neutron dosimetry, $S(\alpha,\beta)$ thermal, neutron multigroup, photoatomic multigroup, and continuous-energy proton (*45*). In MCNPX, the physics module requires the ENDF/B-VII photonuclear data library endf7u. Photonuclear interactions modeled in MCNPX currently rely on new or improved data provided by the ENDF/B-VII photonuclear data library *endf7u*. However, photonuclear data are tabulated by isotope and tables are chosen separately based on the true isotope (by ZA) requested (*44*).

Due to the lack of data and theoretical models for photofission, the ENDF/B-VII photofission library used by MCNPX is primarily based on neutron-induced data (*45*). The model used by MCNPX assumes that target nuclei will produce fission in the same way, regardless of the type of the incident particle. Replacement of the photofission γ-yield with

the neutron-induced fission yield is justified by the fact that once the scission of the target nucleus has taken place, the de-excitation channels of the daughter fragments lose memory about the fission type (*15*).

In 2006, the LANL/T-16 Nuclear Physics Group supported by the X-Division at Los Alamos National laboratory released the Beta version of the ENDF/B-VII photonuclear data library LA150U. LA150U is the only photonuclear data library supported by the X-Division at Los Alamos National Laboratory (*45*). The xsdir file provided for MCNPX installation was modified to include this library to access this photonuclear data library. Both the xsdir file and the data library have to be present in the data file directory specified by the environmental variable DATAPATH. These continuous-energy photonuclear libraries were used as the primary data source for the majority of photofission simulations used throughout this investigation. The specific isotopes identified from evaluated photonuclear data tables are used for photonuclear particle production in MCNPX.

4.2.2 Energy Spectra

In addition to the settings discussed above, in order to enable photofission interactions and secondary emissions, the DG entry on the ACT card must be set to LINES if individual line-amplitude details are desired. This is crucial to the simulation of delayed-fission γ-ray energy spectra. However, enabling this option makes the simulation significantly slower. Information collected from delayed fission γ-rays were recorded using an F4 tally positioned inside the detector cell. The F4 tally card provides a measure of the flux averaged over a cell. The F4 tally was subdivided into energy and time bins using the En and Tn input cards, respectively. The information contained on these cards are used to

describe subdivisions of the tally space into discrete and contiguous increments of the particle energy at the time of scoring. A typical F4 tally card along with its corresponding energy and time cards used for this work is given by

F4:P 3

E4 1E-6 4096I 3

T4 -1 1E8 1E11 T

Here, tally card F4 specifies photon flux averaged over cell 3 in units of particles/cm^2. The energy and time bin structure requires that entries are added in the order of increasing magnitude. Here, the energy card will separate the F4 tally into 4096 energy bins beginning from the energy cutoff to 1E-6 MeV and ending at 3.0 MeV. The time card separates an F4 tally into four time bins: (1) from -∞ to -1.0 shake, (2) from -1.0 shake to 1E8 shake, (3) from 1E8 shake to 1E11 shake, and (4) a total over all time. The energy bins were subdivided with the intent of replicating the energy division parameters set within the Canberra LYNX multichannel analyzer (MCA) used during experimental measurements. The time bin intervals were set to include a time period in which all γ-ray emissions from photonuclear reactions are accounted for. In addition, energy cutoff cards (CUT: p and CUT: n) were used to specify a minimum energy below which each particle is killed. Thus, whenever a neutron or photon falls below the specified energy, it is no longer tracked. This truncation method is generally used to reduce the time per particle history by simplifying the physics used to generate the random walk for each particle. In the simulation models, the technique was used primarily for variance reduction and run-time reduction for recording delayed fission γ-rays. Consequently, the number of particle histories was increased from $1e^9$ to $2e^9$ to account for the inaccuracy of the tally estimate.

4.3 MCNPX Model of Experimental Setup

Following the acquisition of experimental photofission data, a new MCNPX model was built. This model was designed to recreate the experimental cell geometry as used during measurements. Experimental parameters within MCNPX included the shielding materials and materials contained within the beam room cavity during measurements. The geometrical dimensions were directly entered within the code for an accurate 1:1 scale model of the experimental setup. In contrast to the previous MCNPX model, a rectangular detection cell was created outside the target material region to properly recreate the space occupied by one of the HPGe detectors during the experimental measurements. Figure 4-2 shows a visual representation of the redesigned MCNPX model geometry produced in Visual Editor.

The environmental materials represented within this model included: air within the beam room, lead and borated polyethylene shielding the detector, along with ordinary concrete from which the walls were made. The 1.8 m thick concrete wall separating the beam room from the accelerator hall along with the beam port connecting the two was included within this model. The source point was positioned within the accelerator hall and directed inward toward the beam room at the entrance to the beam port. In addition to changes made to the geometry of the environment and the detection region, modifications were made to the energy and time tally characteristics. Because this investigation is interested in β-delayed γ-rays which are expected to enter the detector within the energy range of about 2-3 MeV, a lower energy bound was set at 2.0 MeV to ensure a proper energy cutoff for any γ-ray entering the detection region of the model. The upper bound on

the time tally was extended to 7E6 shake (70 ms) to account for the 67 ms of acquisition time used during the experimental measurements.

4.4 MCNPX Comparison to Experimental Results

4.4.1 Measured γ-rays from ^{232}Th, ^{238}U, and ^{239}Pu

Spectra were plotted in Matlab® and a postprocessing technique was used to smooth the measured spectra. Because of the inherent random nature in the emissions from a γ-radiation source, spectra from acquired γ-ray detection exhibit strong statistical fluctuation (*3*). A 7-point moving average smoothing method whose details can be found in work by M. Alamaniotis (*3*) was used to remove Poisson fluctuation from the measured γ-ray spectra collected during this investigation. This methodology utilizes an interval based smoothing of a spectrum and subsequently suppresses the variance. Figure 4-3 illustrates the use of this SVR-based methodology on the measured γ-ray energy spectrum of ^{238}U.

Figure 4-4 compares spectral distributions of delayed γ-rays from an 18.9 g/cm^2 ^{238}U plate, a 1.0 gram, 19.8 g/cm^2, 60μCi ^{239}Pu sample, and the four 6.0 g/cm^2 ^{232}Th cylinders. Prominent γ-ray signatures collected above 3 MeV indicate the presence of fission fragments unique to each of the target materials. Six independent yields were present in each of the three spectra at similar energy values. These similarities are attributed to the cumulative chain yields for the photofission of these actinides. The cumulative yields are a function of the fissioning nuclei mass number (A). H. Naik et al. studied yields of fission products relevant to mass distributions using bremsstrahlung with end point energies >10 MeV of actinides ^{232}Th, ^{238}U, and ^{239}Pu (*28*). Naik reported higher yields of fission products around mass numbers 133-135 for bremsstrahlung-induced fission of ^{238}U

and ^{239}Pu, and higher yields about mass numbers 143-145 for ^{232}Th. These mass yields thus result in unique energy γ-ray spectra which show similar delayed emissions due to the overlapping trends in their product distributions.

4.4.2 ACE/TENDL Photonuclear Data Assessment of ^{232}Th

Photonuclear data from TENDL/ACE was implemented into the data library of MCNPX. In 2011 and 2012, the IAEA released the TALYS-based evaluated nuclear data library, TENDL, containing evaluations for seven types of incident particles, for nearly 2400 isotopes, up to 200 MeV. TENDL is a nuclear data library which provides the output of the TALYS nuclear model code system for direct use in both basic physics and applications (*46*). Within TENDL, an ACE sublibrary exists which contains data files of incident gamma interactions. These ACE files are of primary interest to this project in that they provide data on a number of isotopes, not supported through the ENDF/B-VII photonuclear data library. Table 4-1 lists the 45 isotopes (A≥175) containing incident gamma data provided by the TENDL/ACE data library.

Although this new set isotopes contains what appears to be a new and robust set of data, it was extracted specifically for the ^{232}Th element which is unavailable through the ENDF/B-VII photonuclear library. The actinides ^{235}U, ^{238}U, and ^{239}Pu were imported without modifications from ENDF/B-VII.1 released by the X-Division at Los Alamos National Laboratory (*46*). To implement the TENDL/ACE data into MCNPX, the ACE files were downloaded from the TENDL-2011 website and placed within the data directory. Next, the filename and route were modified for each desired ACE *xsdir* file. An example *xsdir* file modification for ^{232}Th is shown below. The *xsdir* file as downloaded from TEDNL has the following format:

90232.00u 230.044800 filename route 1 1 66649 0 0 0.000E+00

The filename needs to be set to correctly match the ACE file name within the MCNP directory. The route entry is related to putting different data files in different directories. This feature is no longer supported and must be set to zero. Entry 5, on the *xsdir* line, says the data are type 1 ASCII format (as opposed to binary). Entries 6 and 7 tell MCNP where to look within the file (filename) for data. They are pointers related to relative position of data. Therefore, the TENDL/ACE file must not be copied into *endf7u* as none of the new data will work. Thus, the TENDL/ACE file is kept as a separate file within the directory, namely, Th232-g_ace, in this example. Making these changes, the ACE *xsdir* line becomes:

90232.00u 230.044800 Th232-g_ace 0 1 1 66649 0 0 0.000E+00

This line can then be placed at the end of the existing *xsdir* file in the MCNP data directory. After modification, these files are added to the material card of an input file. As shown in Figure 4-5, the simulation of ^{232}Th using the TENDL library correctly predicts few photo peaks below 3 MeV. In the energy range from 3-5.5 MeV several measured peaks are predicted using the TENDL library. These delayed γ-rays above 3 MeV are unique to the fission fragments emitted from ^{232}Th. While discrepancies exist between the simulated spectra and measured spectrum, the spectrum produced using the TENDL library closely aligns with a number of the measured energy peaks. Such alignment is not present in the spectrum produced using the ENDF/B-VII library.

4.4.3 Spectral Analysis of ^{238}U, and ^{239}Pu

Figure 4-6 shows a comparison of measured and simulated energy spectra from ^{238}U in the region above 3 MeV. This overlaying and offsetting of measured spectra with a calculated spectrum facilitate the identification of correctly predicted photopeaks within

the energy range of 2910 keV to 4390 keV. The same energy spectrum measured with a commercially available MCA (Canberra LYNX) was included for comparison in Figure 4-6 and it can be observed that the energy resolution achieved using the customized spectrometry system is similar to the results obtained with the commercial MCA system.

The simulated energy spectrum of ^{238}U correctly identifies several photopeaks as compared to the measured data acquired using the Genie2000 software and the list-mode system. While several peaks in the simulated spectrum align with the measured spectra, measured photopeaks from ^{84}Br (3927 keV), ^{88}Br (3932 keV), and ^{90}Rb (4135 keV) are not present in the simulated spectrum. Reedy et al. reported the prediction of similar photopeaks from 22 MeV neutron-induced fission of ^{238}U (*13*). These predictions include identification of ^{98}Y (2941 keV), ^{108}Tc (2946 keV), ^{98}Y (3228 keV), ^{97}Y (3288 keV), ^{98}Y (3310 keV), ^{97}Y (3401 keV), ^{93}Rb (3458 keV), ^{95}Y (3576 keV), ^{91}Rb (3600 keV), ^{91}Rb (4078 keV), ^{90}Rb (4135 keV), and ^{90}Rb (4366 keV). Similar peak predictions between these data sets indicate small variability between neutron-induced and photon-induced energy spectra from ^{238}U.

For the photofission of ^{238}U, Wehe et al. reported measuring similar products at energies above 3 MeV from bremsstrahlung at 9-MeV end point energies (*11*). Identification of these photofission products was approximated by the neutron-induced fission products yields of ^{238}U. P. Sibczynski et al. reported measuring delayed γ-rays at ^{95}Y (3576.0 keV) and ^{84}Br (3927.5 keV) from 15-MeV bremsstrahlung-induced fission of 93% enriched ^{235}U (*47*). The measurements were taken after 10-minute irradiation/30-minute cooling intervals over a 24-hour period. While Sibczynski's observations result

from photofission of enriched ^{235}U, these photopeaks were found in the experimental data from photofission of ^{238}U.

Figure 4-7 shows a comparison of measured and simulated spectral distributions of delayed γ-rays from ^{239}Pu photofission in the region from 3-6 MeV. Several of the measured γ-ray peaks were correctly predicted in the simulated spectrum. Predicted energy peaks at 3.08 MeV, 3.12 MeV, 3.52 MeV, and 4.43 MeV are shown to closely align with prominent peaks in the measured spectrum. Fission yields have not yet been associated to the energy peaks identified from the measured spectrum.

Campbell et al. identified high-energy γ-rays in a range from 3.2 MeV to 3.6 MeV due to thermal neutron-induced fission of ^{235}U and ^{239}Pu (*48*). Delayed γ-rays from ^{239}Pu were attributed to the fission fragments ^{136}Te (3235 keV), ^{106}Tc (3260 keV), ^{97}Y (3288 keV), ^{90m}Rb (3317 keV), ^{97}Y (3401 keV), ^{90}Rb (3458 keV), ^{95}Y (3576 keV), and ^{91}Rb (3600 keV). In view of the above observations, the ^{97}Y (3288 keV) can be identified from both the experimental and simulated spectra. Although a significant quantity of prominent energy peaks exist within the present data, little information is provided in the region above 4.5 MeV.

4.5 Composition Analysis in MCNPX

Yields of various products from bremsstrahlung-induced fission of actinides ^{232}Th, ^{238}U, and ^{239}Pu can be analyzed to determine the isotopic composition of a sample containing one or more fissionable isotopes. Several techniques utilizing fission-based γ-ray peak intensity ratios for the identification and quantification of the relative concentration of nuclei in a sample have been extensively studied in the past *(13, 23, 25, 26)*. For example, the *discrimination ratio*, measured as the intensity ratio between the ^{97}Y

(1103 keV) peak and the ^{89}Rb (1032 keV peak), were observed to be significantly different between ^{235}U, ^{239}Pu, and ^{238}U *(49, 50)*. Observations like this can be utilized to measure isotopic composition in nuclear material samples. The following study was performed to evaluate the sensitivity of simulation models used throughout the investigation and in no way aims to recreate or take credit for the techniques used therein.

Models containing different concentrations of ^{235}U/^{238}U were simulated in MCNPX. The predicted spectra used the ENDF/B-VII photonuclear data library provided by MCNPX and the IAEA TALLYS-based photonuclear library, TENDL/ACE. The concentrations included 0%, 10%, 50%, 90%, and 100% ^{235}U. The predicted energy spectra from pure samples of ^{238}U and ^{235}U resulted in notable similarities between energy peaks. The spectra were then mapped onto one another to emphasize the convolution of energy peaks. The overlapped energy spectra of the pure uranium materials indicate specific sum peak contributions of the uranium mixture. The sum of these energy peaks at 1.60 MeV, 2.39 MeV, and 3.29 MeV were used to determine the isotopic composition for both ^{238}U and ^{235}U fissionable isotopes.

The spectra shown in Figure 4-8 and Figure 4-9 represent the simulated energy spectra produced using pure concentrations of ^{235}U and ^{238}U. The sum of these two spectra, shown in Figure 4-10, represents the expected spectrum produced from using a mixture of these pure concentrations. By identifying an individual peak from this mixed uranium spectrum, which remains uniform regardless of the concentrations of either ^{235}U or ^{238}U, a measure of the total fission events in the sample can be determined. This uniform peak is used fiducially. In contrast, a signal peak is identified which increases or decreases based on the relative concentrations of each mixture. The signal peak must follow a unique trend

in response to the fluctuating concentrations of either ^{235}U or ^{238}U, in this case. Once fiducial and signal peaks are identified, the ratio of their areas can be used as a concentration measure of the contributing signal peak's source. This technique of Peak Ratio Analysis is a simplistic method used to approximate isotopic concentrations of a sample containing two or more fissionable isotopes. Figure 4-11 and Figure 4-12 illustrate the increasing trend of the energy peak as ^{235}U concentrations are increased.

Identifying the summation of peak ratios in each pure sample provides a quantity which is then set equal to the peak ratio of the mixture. Repeating this step for two additional energy peaks allows for the formation of a set of two equations with two unknowns. For example, using the three energy peaks indicated in Figure 4-10, the following equations are solved to find the ^{238}U and ^{235}U concentrations within the mixture:

$$\left(\frac{peak\ 1}{peak\ 2}\right)_{mixture} = C_1\left(\frac{peak\ 1}{peak\ 2}\right)_{238} + C_2\left(\frac{peak\ 1}{peak\ 2}\right)_{235} \quad [4\text{-}2]$$

$$\left(\frac{peak\ 1}{peak\ 3}\right)_{mixture} = C_1\left(\frac{peak\ 1}{peak\ 3}\right)_{238} + C_2\left(\frac{peak\ 1}{peak\ 3}\right)_{235} \quad [4\text{-}3]$$

where the coefficients C_1 and C_2 indicate the quantity of each pure uranium isotope within the mixture. These equations can then be solved given the known values of each energy peak. From the simulated energy spectra shown in Figure 4-11 and Figure 4-12, the 2.39 MeV and 3.29 MeV peaks are used as signal peaks. A well-defined variation in the peak heights are shown. The energy peak at 1.60 MeV is then used as the fiducial. Although this fiducial peak does not sustain constant amplitude among the concentrations, it has the least amount of variation shown throughout each spectrum. Figure 4-13 shows the relative ^{235}U concentration as a function of the peak ratio. As the concentration of ^{235}U is varied in each model, the ratio between the peaks change, indicating a linear relationship. Reedy et al.

generated peak ratio as a function of relative ^{238}U concentration for targets containing mixed samples of ^{238}U and ^{232}Th. Results pertaining to a similar linear relationship in the data and error resulting from difficulties in peak fitting were reported (*7*).

Although this method of isotopic analysis has proven useful in this approximation, uncertainties within the MCNPX simulations still exist. Uncertainties may be attributable to discrepancies in the number of scored particles during the Monte Carlo calculations. Increasing the number of counted particles during the simulation is a widely used variance reduction technique. These calculated energy spectra were produced from the scoring of 10^6 source particle histories within the simulation detector region. Resolved counting uncertainties were observed in calculations involving an increase in source particle histories on the order of 10^9.

Peak ratio analysis using the 4-π detector geometry resulted in errors that averaged nearly 20% for each concentration. This deviation from the true relative concentration of ^{238}U was predominantly due to both signature and fiducial peaks being convolutions of multiple fission fragments in the simulated spectra. In addition, the small number of data points collected for this evaluation may have caused statistical inaccuracies leading to these associated errors. This example demonstrates how the use of two closely positioned peaks can lead to large statistical error. The variance in this example verifies that the fiducial peak is not truly constant regardless of the mixtures relative concentration. This method of peak ratio analysis was repeated for eight separate mixture concentrations of ^{235}U using the experimental setup model in MCNPX. Concentrations of ^{235}U used in these models ranged from 10% to 80%.

Figure 4-14 shows the relationship between the calculated concentration and the true relative concentration of ^{235}U for a set of eight scenarios. This analysis used a 2.29 MeV energy peak as the signature peak and a 1.60 MeV energy peak as the fiducial peak. The average error was approximately 5% at 10% relative ^{235}U concentration and 17% at 80% relative ^{235}U concentration. Although a decrease in the associated errors exists between the different simulation models, the error is still too large to make this a useful approximation.

Table 4-1. List of nuclides containing photonuclear data from the TENDL/ACE nuclear data library. This list includes ^{232}Th, which is not provided in the ENDF/B-VII library.

^{176}Au – ^{205}Au	^{143}Dy – ^{169}Dy	^{145}Ho – ^{172}Ho	^{168}Os – ^{196}Os	^{253}Rf – ^{263}Rf
^{198}At – ^{223}At	^{255}Db – ^{263}Db	^{179}Hg – ^{208}Hg	^{175}Pt – ^{202}Pt	^{263}Sg – ^{266}Sg
^{214}Ac – ^{234}Ac	^{135}Eu – ^{162}Eu	^{269}Hs – ^{277}Hs	^{185}Pb – ^{214}Pb	^{150}Tm – ^{177}Tm
^{232}Am – ^{247}Am	^{146}Er – ^{175}Er	^{171}Ir – ^{198}Ir	^{195}Po – ^{218}Po	^{160}Ta – ^{186}Ta
^{190}Bi – ^{218}Bi	^{241}Es – ^{257}Es	^{157}Lu – ^{184}Lu	^{231}Pu – ^{247}Pu	^{180}Tl – ^{210}Tl
^{238}Bk – ^{251}Bk	^{204}Fr – ^{232}Fr	^{253}Lr – ^{262}Lr	^{226}Pa – ^{239}Pa	^{224}Th – ^{238}Th
^{266}Bh	^{245}Fm – ^{259}Fm	^{246}Md – ^{260}Md	^{165}Re – ^{192}Re	^{227}U – ^{242}U
^{237}Cf – ^{256}Cf	^{135}Gd – ^{165}Gd	^{232}Np – ^{244}Np	^{201}Rn – ^{228}Rn	^{179}W – ^{190}W
^{238}Cm – ^{250}Cm	^{154}Hf – ^{186}Hf	^{252}No – ^{259}No	^{207}Ra – ^{234}Ra	^{151}Yb – ^{180}Yb

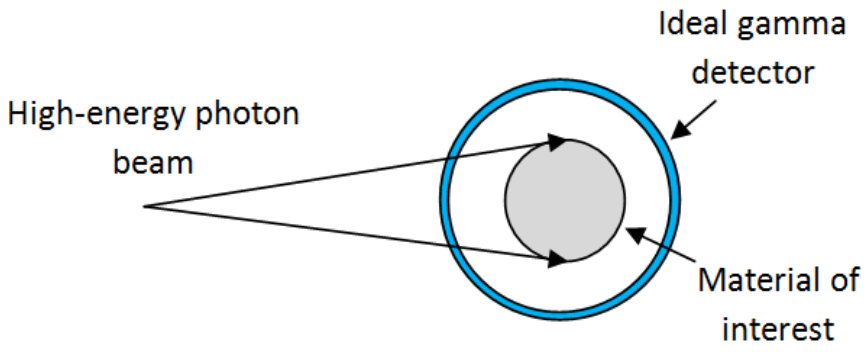

Figure 4-1. Illustration of MCNPX simulation 4-π detection geometry. Spherical region encompasses target material for ideal detection capability.

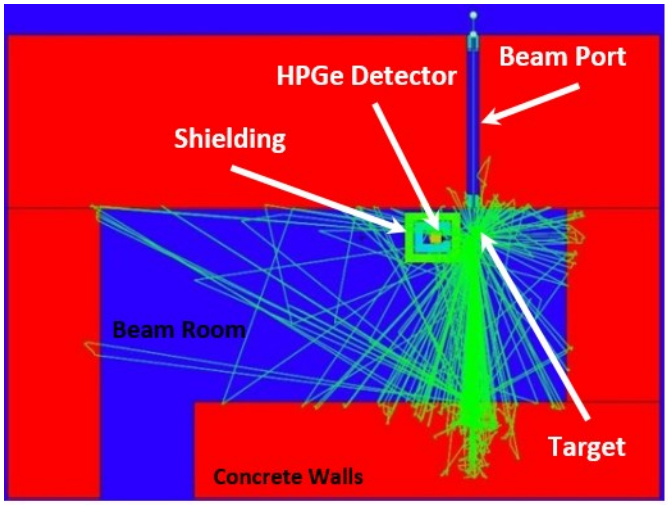

Figure 4-2. Visual representation of the experimental cell geometry in MCNPX. The green traces shown here are symbolic of the γ-rays produced during the MCNPX simulation.

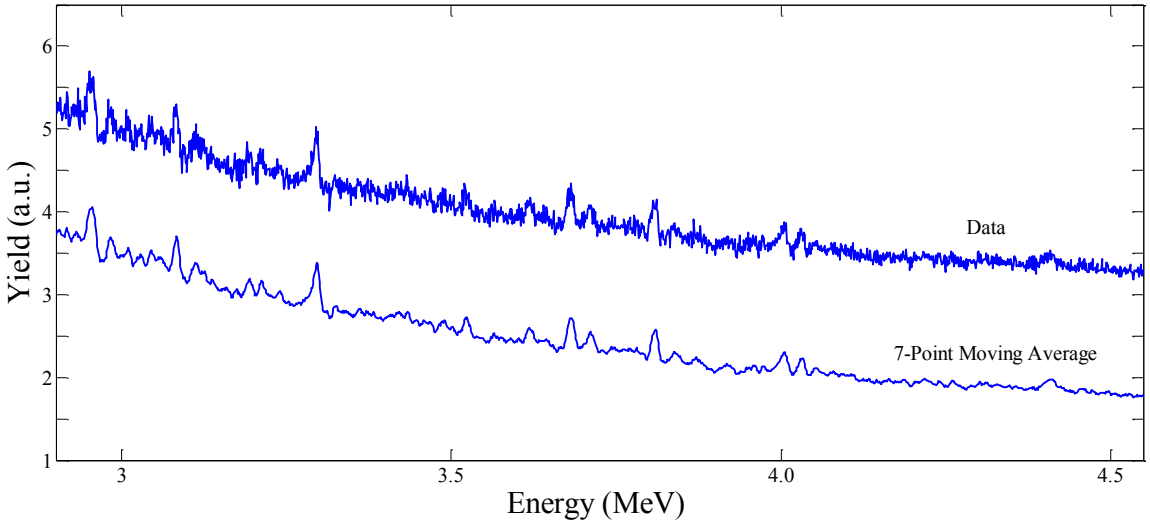

Figure 4-3. SVR-based moving average smoothing function (*3*) applied to γ-ray spectrum collected with high-resolution germanium detector. Spectra are offset to emphasize the effect of the smoothing function. Each photo peak in the smoothed spectrum is preserved while the noise is removed producing a higher resolution image.

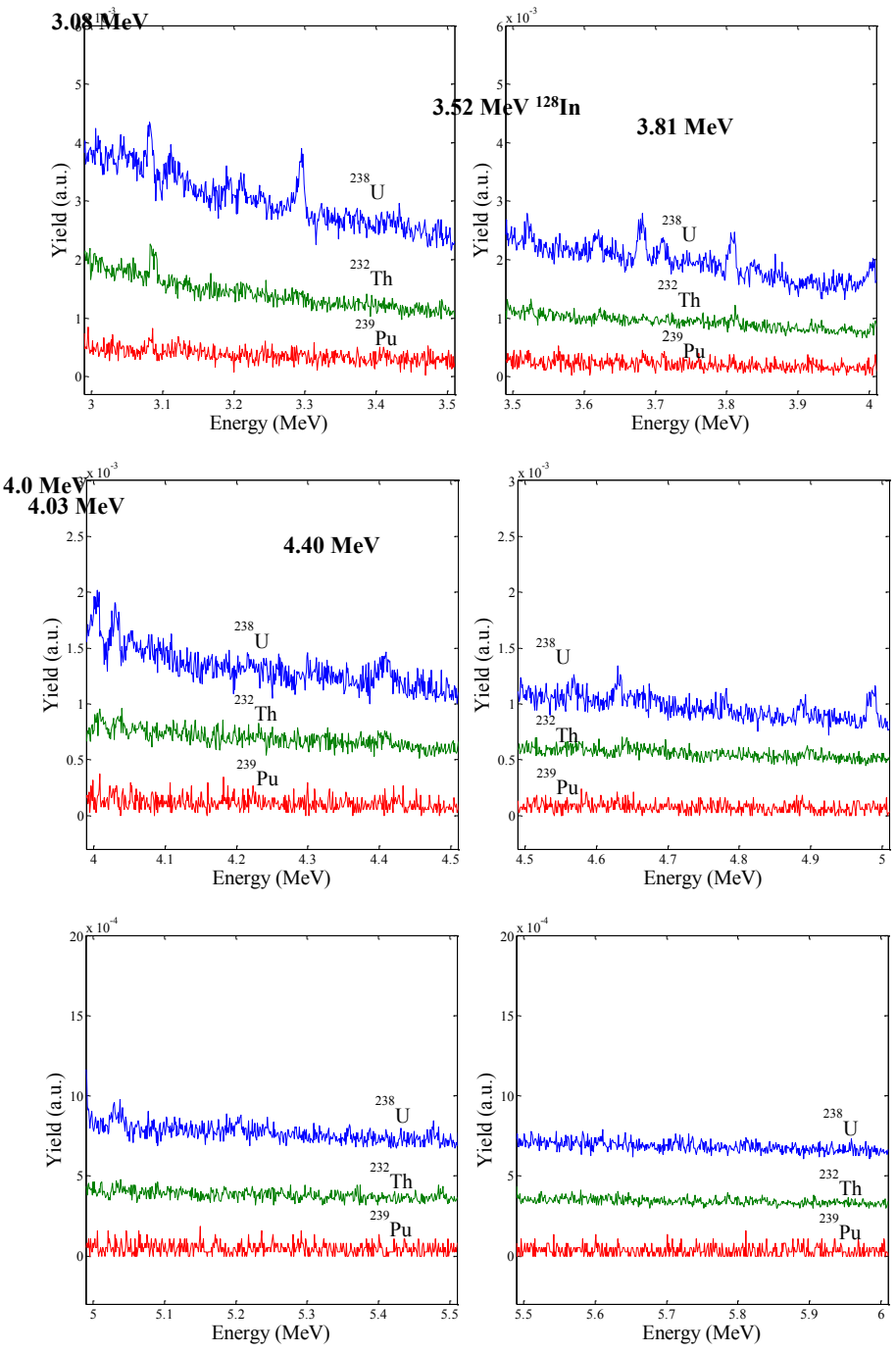

Figure 4-4. Energy spectra of 18.9 g/cm^2 ^{238}U plate; a 1.0 gram, 19.8 g/cm^2, 60μCi ^{239}Pu sample; and four 6.0 g/cm^2 ^{232}Th cylinders measured with a Fast ComTec list mode system. Spectra were produced using a 22 MeV bremsstrahlung beam pulse of 150nC at 15Hz. Data from the first 10 ms following each LINAC pulse were removed. The ^{238}U plate was irradiated for two hours, the ^{239}Pu sample was irradiated for 100 minutes, and the ^{232}Th cylinders were irradiated for three hours. Delayed γ-rays above 3 MeV that are present in all three measured spectra are labeled accordingly. Similarities among spectra are indicated up to approximately 4.4 MeV.

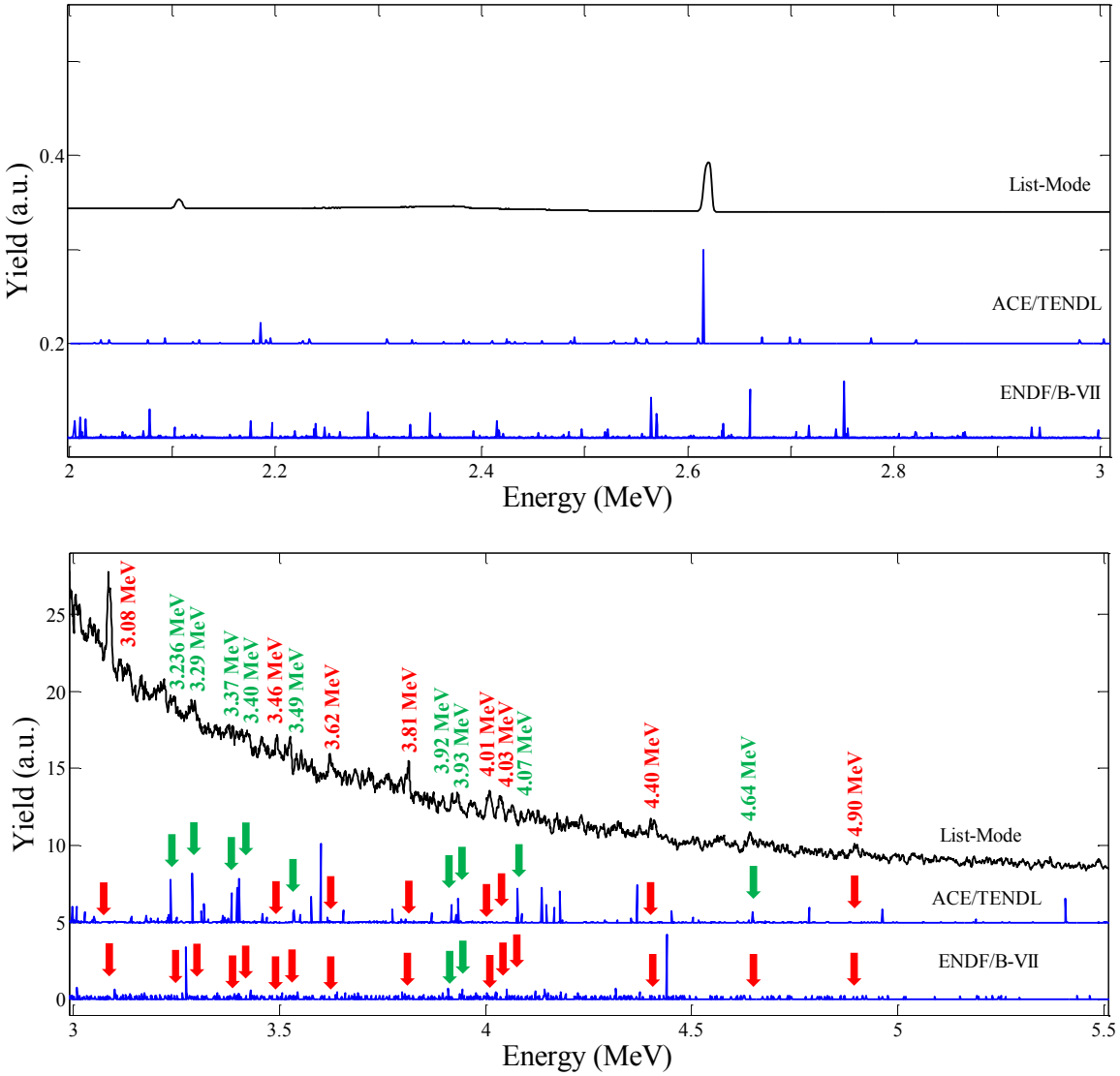

Figure 4-5. Energy spectrum from 6.0 g/cm^2 ^{232}Th cylinders irradiated for three hours using a bremsstrahlung beam pulse of 150nC at 15Hz and measured with a Fast ComTec list mode system. Spectrum is compared to predicted energy spectra using both the ENDF/B-VII and TENDL/ACE photonuclear data libraries in MCNPX. The TENDL library was added to the experimental cell geometry model.

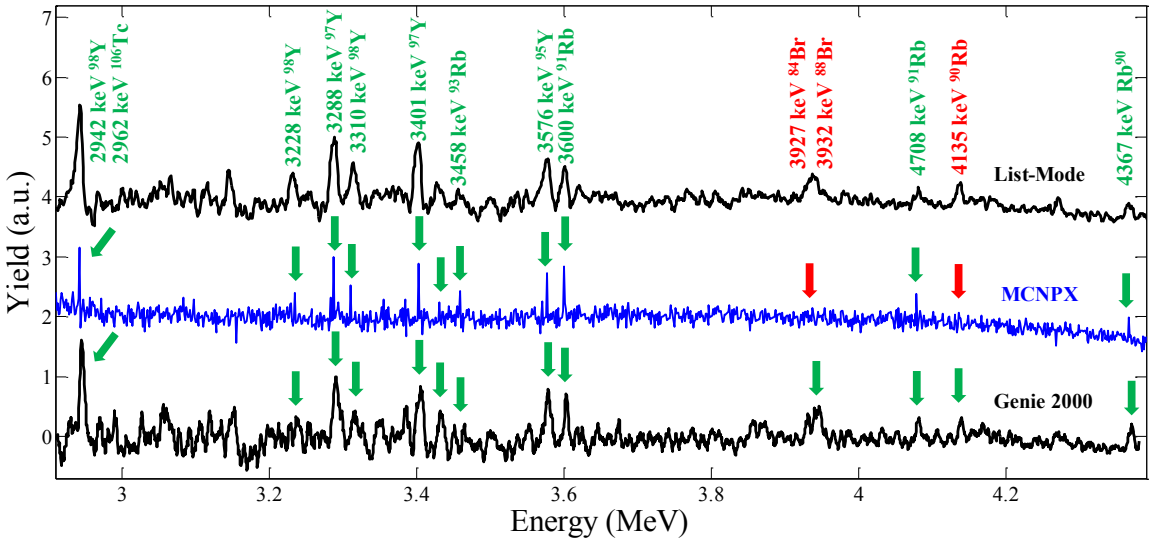

Figure 4-6. Comparison of measured and predicted delayed fission γ-ray spectra from 18.9 g/cm^2 ^{238}U plate (enriched to 0.2% ^{235}U), irradiated for two hours using a 22 MeV bremsstrahlung beam pulse of 150nC at 15Hz. Labeled photopeaks in green indicate the presence of correctly estimated fission fragments. The predicted spectrum was created using MCNPX and is compared to measured spectra from the Genie2000 acquisition software and a list-mode system. The Simulated spectrum is shown in blue and is offset to emphasize the differences in each spectrum.

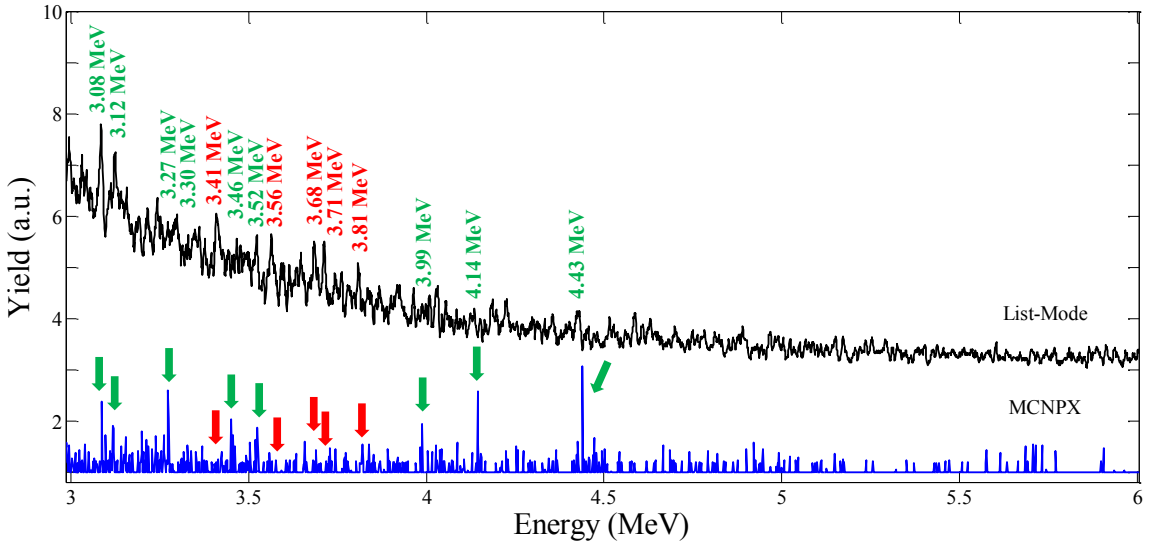

Figure 4-7. Energy spectra from 60μCi ^{239}Pu sample, irradiated for 100 minutes using a 22 MeV bremsstrahlung beam pulse of 150nC at 15Hz. The Simulated spectra are shown in blue and are offset to emphasize the differences in each spectrum. Labeled photopeaks in green indicate the presence of correctly estimated fission fragments.

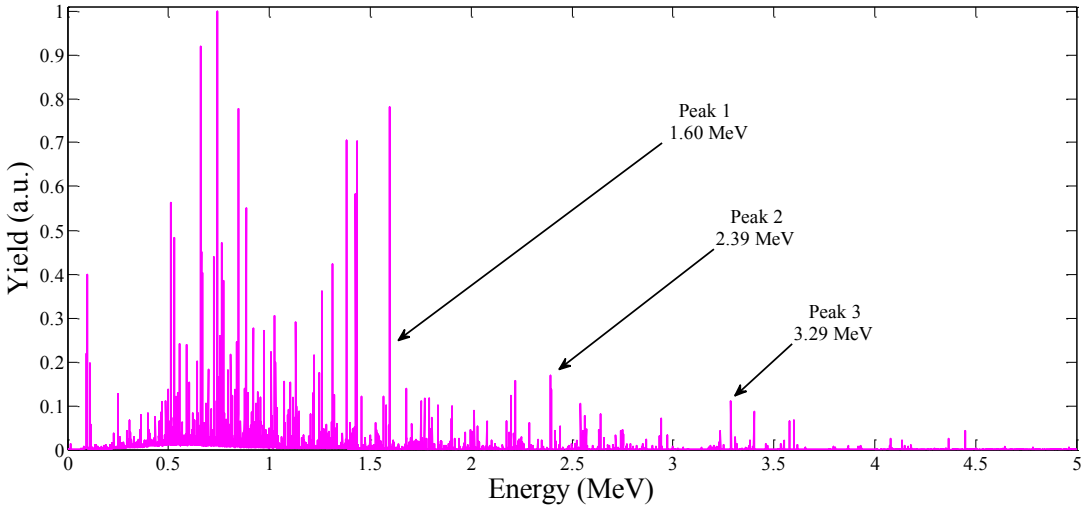

Figure 4-8. Predicted overlapping delayed fission γ-ray spectra from 0 MeV to 5.0 MeV for pure ^{235}U using the ENDF/B-VII library and simplified simulation geometry.

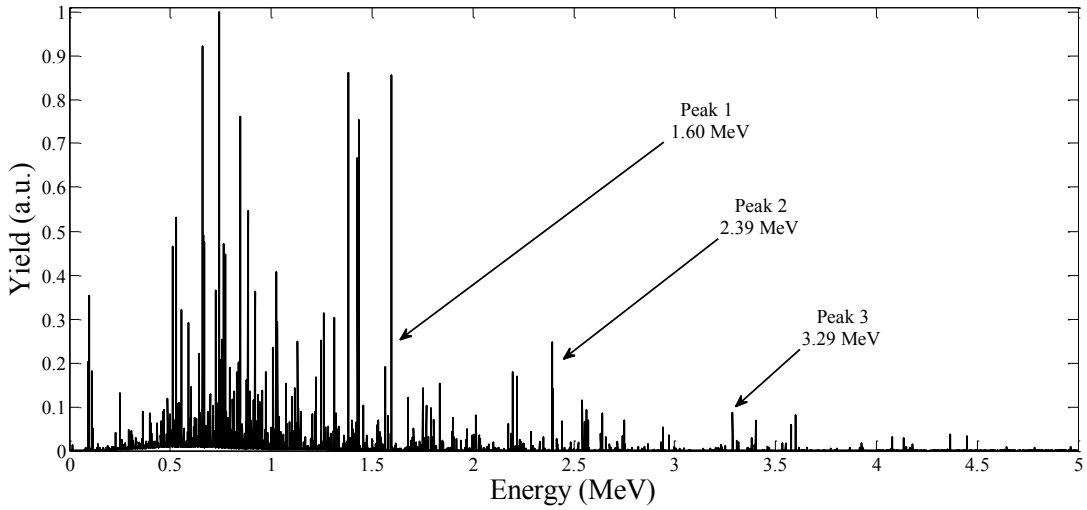

Figure 4-9. Predicted overlapping delayed fission γ-ray spectra from 0 MeV to 5.0 MeV for pure ^{238}U using the ENDF/B-VII library and simplified simulation geometry.

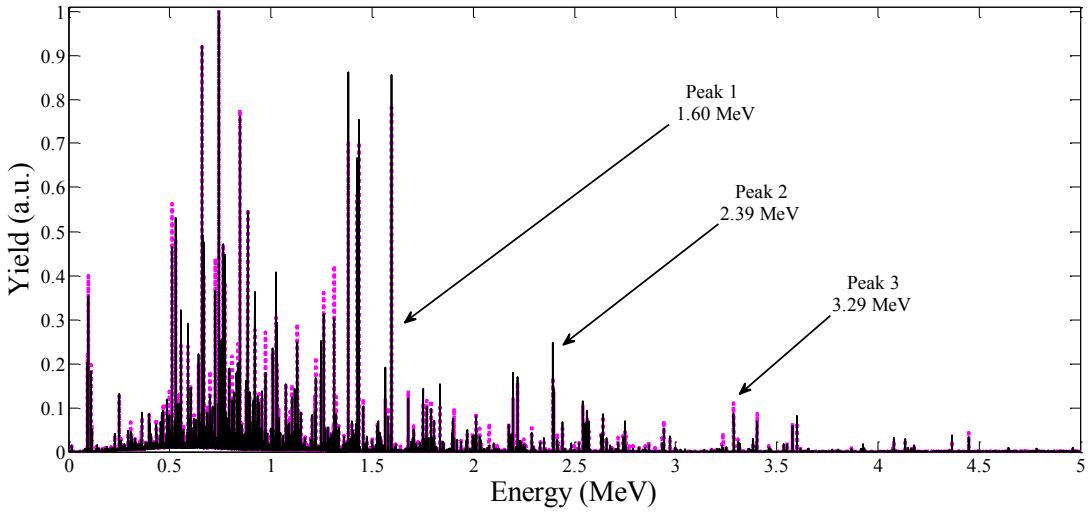

Figure 4-10. Predicted overlapping delayed fission γ-ray spectra from 0 MeV to 5.0 MeV for pure mixtures of ^{235}U (blue spectrum) and ^{238}U (red spectrum) using the ENDF/B-VII library and simplified simulation geometry.

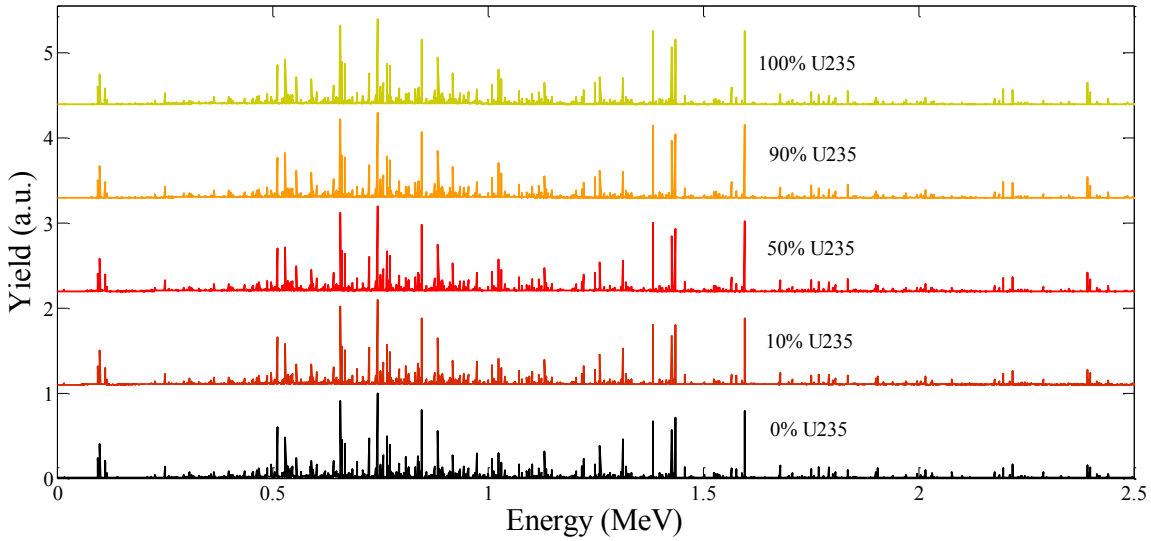

Figure 4-11. Predicted delayed fission γ-ray spectra from 0 MeV to 2.5 MeV for different concentrations of $^{235}U/^{238}U$ mixtures using the ENDF/B-VII libraries and 4-π detector geometry.

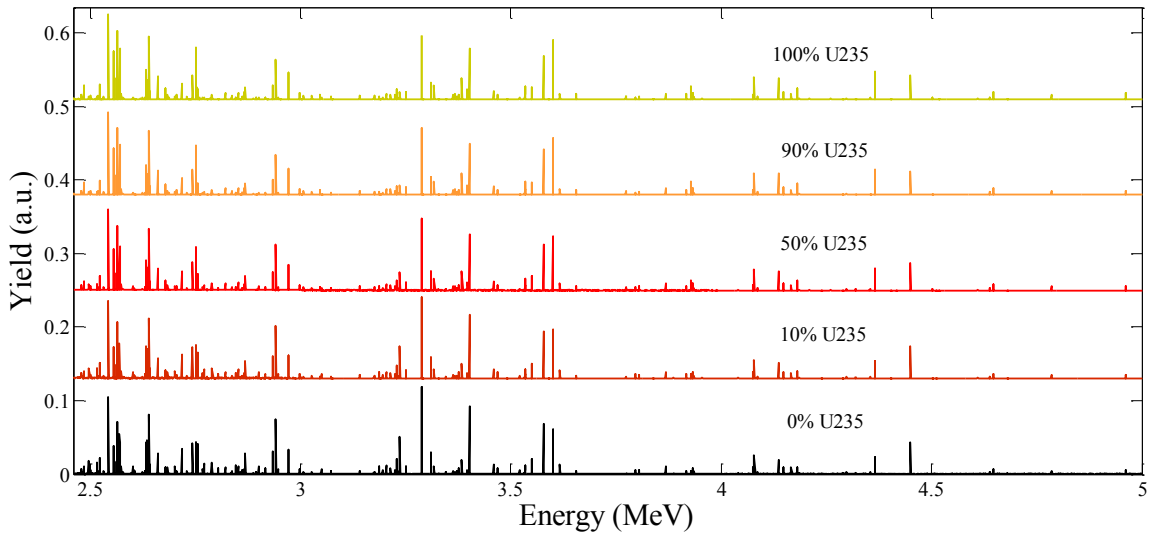

Figure 4-12. Predicted delayed fission γ-ray spectra from 2.5 MeV to 5.0 MeV for different concentrations of $^{235}U/^{238}U$ mixtures using the ENDF/B-VII libraries and 4-π detector geometry.

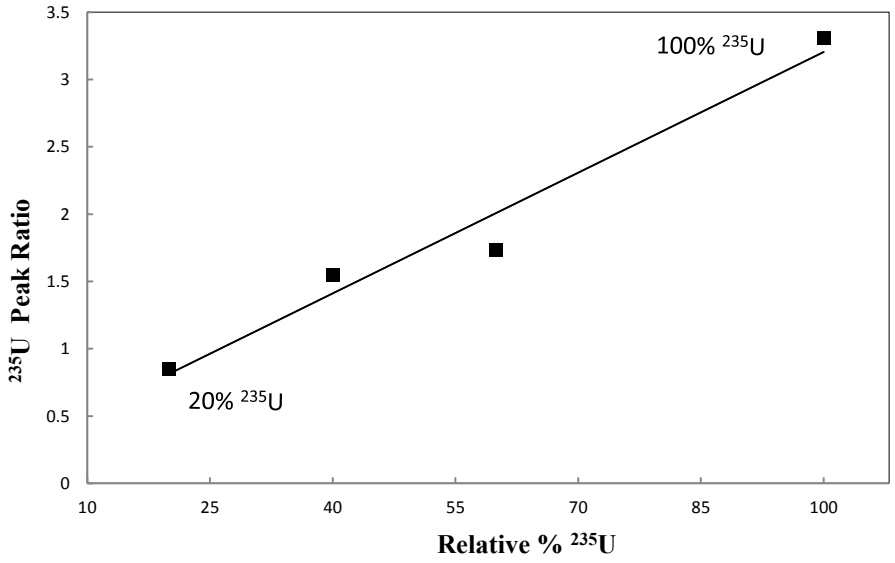

Figure 4-13. Ratio of signature to fiducial vs. concentration of ^{235}U in a $^{235}U/^{238}U$ mixture using 4-π simulation geometry. As the concentration of ^{235}U varies in the mixtures, the ratio between the peaks change and can be described by this linear relationship.

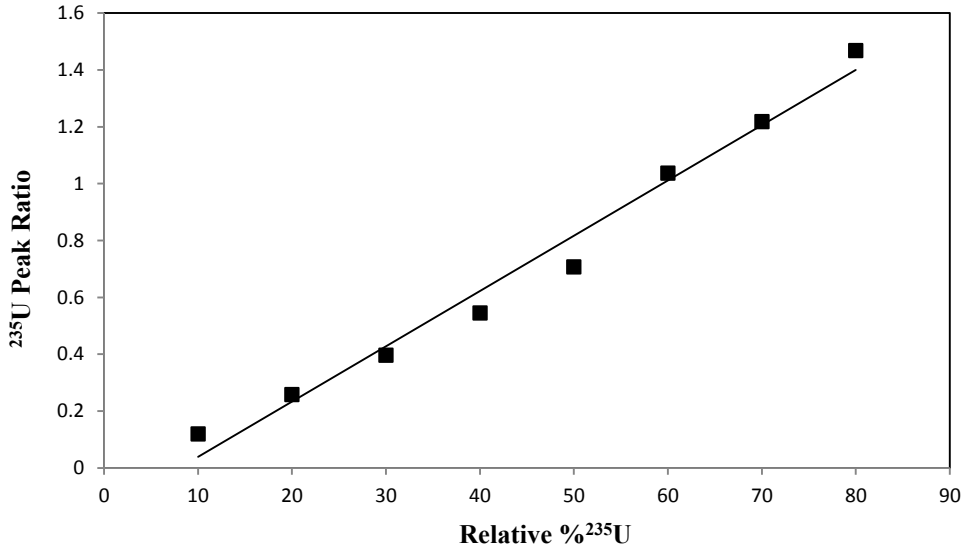

Figure 4-14. Ratio of signature to fiducial vs. concentration of ^{235}U in a $^{235}U/^{238}U$ mixture using the experimental setup geometry in MCNPX. As the concentration of ^{235}U varies in the mixtures, the ratio between the peaks change and can be described by this linear relationship.

CHAPTER 5

CONCLUSIONS AND FUTURE WORK

5.1 Significance of Findings

Experimental photofission data was obtained from the interrogation of actinides ^{238}U, ^{239}Pu, and ^{232}Th using bremsstrahlung with endpoint energy of 22 MeV. An active interrogation technique based on the time and energy characteristics of signature delayed γ-ray signals following photon-induced fission events was investigated. Delayed signatures measured from high-energy γ-ray-induced reactions provide information for isotope identification and quantification of interrogated nuclear materials. Measured energy spectra from ^{239}Pu show γ-rays detected at energies above 3 MeV for time >20 ms between irradiation pulses. Energy spectra collected from ^{232}Th and ^{238}U during times >10 ms between irradiation pulses also resulted in γ-rays detected above 3 MeV. In addition, γ-ray signals collected 10 ms after each LINAC pulse were removed to eliminate any potential interference from neutron-capture interactions. These results provide sufficient evidence to identify these emissions as β-delayed γ-rays from short-lived fission fragments.

Experimentally measured energy spectra were used as a benchmark comparison for energy spectra produced in MCNPX 2.7.0. The photonuclear interaction capabilities of MCNPX were demonstrated in this investigation. Photonuclear data tables were implemented into MCNPX from two different sources and evaluated for their accuracy when compared to the experimental data. As shown in Figure 5-1, the simulation results

provided consistent peak alignment with the measured energy peaks from delayed γ-rays in the energy range from 2.5 MeV to 4.2 MeV.

Notable γ-ray energy lines in the measured spectrum of ^{232}Th were found to be missing from the simulation results and emphasis on the limited availability and accuracy of the ENDF/B-VII photonuclear data was made. Photonuclear data libraries for ^{232}Th were accessed from TENDL/ACE and implemented into the MCNPX data directory. Energy spectra produced from the ENDF/B-VII data were compared to spectra produced from TENDL/ACE data. Results from this comparison indicate discrepancies within the ENDF/B-VII library, specifically endf7u. Figure 5-2 illustrates the differences between these simulated spectra by comparing them to the measured results.

5.2 Limitations and Future Work

The simulation technique used in this investigation proves effective for targets containing ^{238}U, ^{239}Pu, and ^{232}Th. Although the predicted energy spectra are shown to align well with the measured energy peaks, further investigation is needed to determine the accuracy of the peak predictions. In addition, further analysis of the ^{238}U/^{235}U mixtures in MCNPX may be carried out using the method of spectral contribution analysis (SCA). This method focuses on a region of the energy spectrum which spans multiple photopeaks rather than individual peaks as done using peak ratio analysis. The energy spectra from a region can then be easily deconvoluted into their base components. Using superposition, a portion of an energy spectrum (ϕ) from the photofission of a mixed target can be described using the contributing energy spectra of ^{238}U and ^{235}U as a basis set in the equation,

$$\phi = \alpha_{238}\phi_{238} + \alpha_{235}\phi_{235} \tag{5-1}$$

where ϕ_{238} and ϕ_{235} indicate the contributing portion of each energy spectrum and where α_{238} and α_{235}indicate the quantity of each isotope in the target. Thus, this method allows the intensity (α_{235} andα_{238}) of each contributing spectrum to be solved for from its base components. Due to each photofission energy spectra of containing its own unique fission fragment distribution, the resulting intensity parameters indicate the spectral contribution from the photofission of each component. This technique will allow for a direct comparison of the relative concentrations in each model by utilizing regions of the energy spectra instead of individual peak values. In addition, discrimination ratios can be formed from multiple peak pairs in order to enhance the confidence in the material identification (*23*). By providing peak sampling over a range of energies, a better approximation of peak yields is achieved.

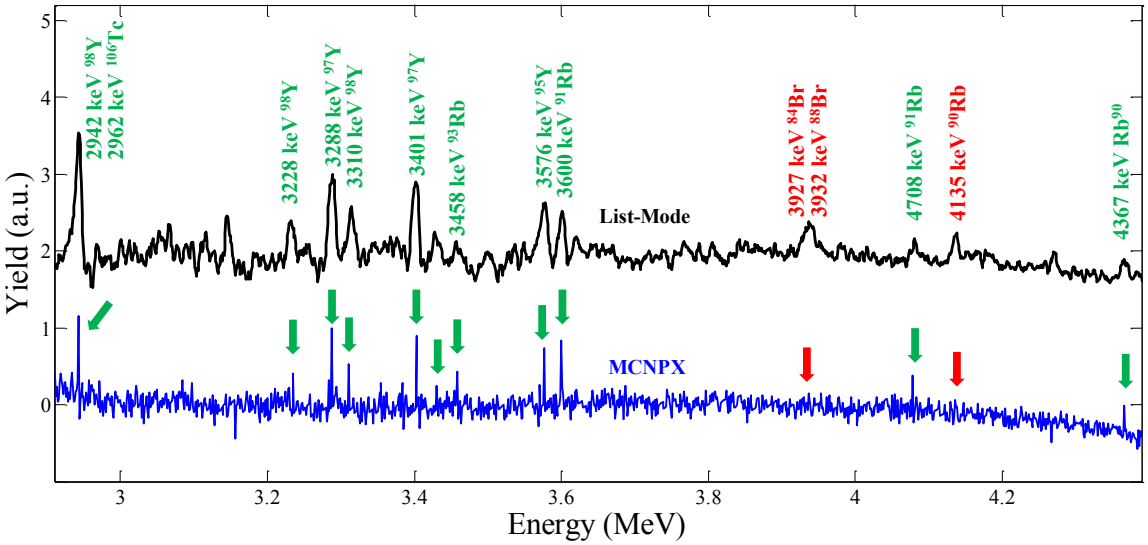

Figure 5-1. Measured and predicted spectral distribution of delayed γ-rays from 18.9 g/cm^2 ^{238}U plate (enriched to 0.2% ^{235}U), irradiated for two hours using 22 MeV bremsstrahlung. Labeled photopeaks in green indicate the presence of correctly estimated fission fragments. The predicted spectrum was created using MCNPX and is compared to measured spectra from a list-mode system. The Simulated spectrum is shown in blue and is offset to emphasize the differences in each spectrum.

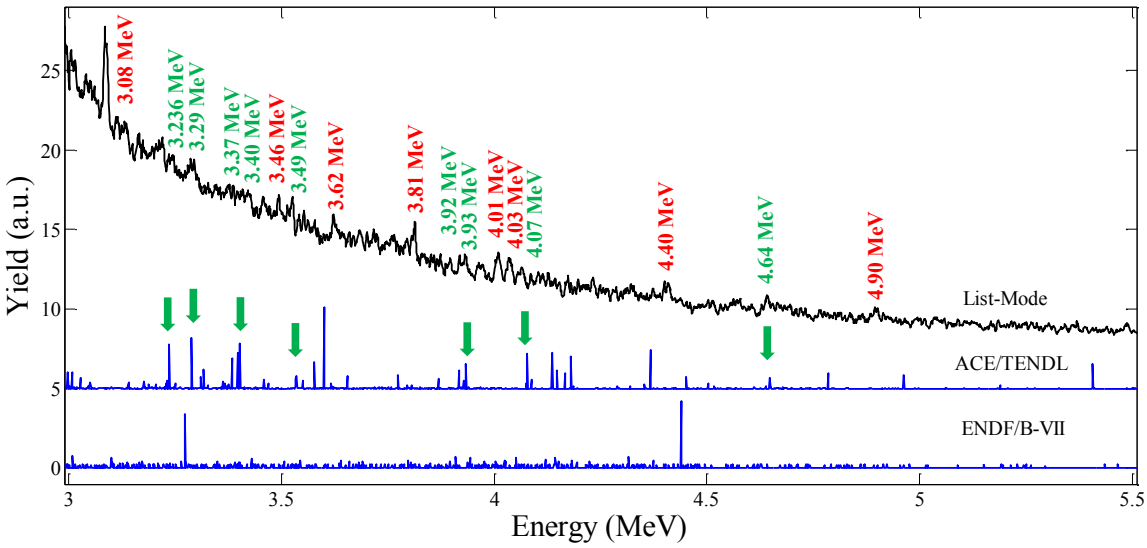

Figure 5-2. Comparison between measured and calculated delayed γ-ray energy spectra from 6.0 g/cm^2 ^{232}Th. The calculated spectra were produced using ENDF/B-VII and TENDL/ACE photonuclear data libraries in MCNPX. Photopeaks labeled in green indicate the presence of correctly estimated fission fragments using the TENDL/ACE library.

APPENDIX A

MCNPX INPUT FILE FOR 4-Π DETECTOR GEOMETRY

```
C DELAYED GAMMA / EXPERIMENTAL SETUP
1 1 -11.7 -1     IMP:N = 1 IMP:P = 1
2 0 1 -3         IMP:N = 1 IMP:P = 1
3 0 3 -4         IMP:N = 1 IMP:P = 1
4 0 4 -2         IMP:N = 1 IMP:P = 1
5 0 2            IMP:N = 0 IMP:P = 0

1 SO 5
2 SO 100
3 SO 10 $ DETECTOR SPHERE
4 SO 11 $ DETECTOR SPHERE

MODE P N
SDEF POS = -10 0 0
     VEC = 1 0 0
     DIR = D1
     PAR = 2
     ERG = 22
     TME = 0
SI1 0.89 1
SP1 0 1
M1 90232 1.0
PHYS:P J J J 1 J J 0
ACT FISSION = P
DG = LINES
F4:P 3
E4:P 1 4096I 6
NPS 1E9
```

APPENDIX B

MCNPX INPUT FILE FOR EXPERIMENTAL SETUP GEOMETRY

```
C DELAYED GAMMA / EXPERIMENTAL SETUP

7 5 -0.92 -7 -8 9          TRCL=3 IMP:N=1 IMP:P=1 $DETECTOR
1 1 -0.00129 -1 #7         TRCL=3 IMP:N=1 IMP:P=1 $DETECTOR CASE
2 1 -0.00129 -2            TRCL=3 IMP:N=1 IMP:P=1
3 2 -11.3 -3 1 2           TRCL=3 IMP:N=1 IMP:P=1 $LEAD
4 3 -1.1 -4 1 2 3          TRCL=3 IMP:N=1 IMP:P=1 $BORATED POLY
5 2 -11.3 -5               TRCL=3 IMP:N=1 IMP:P=1
6 4 -19.1 -6               TRCL=1 IMP:N=1 IMP:P=1 $TARGET
8 6 -2.3  -11 12           TRCL=2 IMP:N=1 IMP:P=1 $WALL
15 2 -11.3 20 -18 -12 22   TRCL=2 IMP:N=1 IMP:P=1
16 1 -0.00129 20 -18 -22   TRCL=2 IMP:N=1 IMP:P=1
17 2 -11.3 -21 19 -12 23   TRCL=2 IMP:N=1 IMP:P=1
18 1 -0.00129 -21 19 -23   TRCL=2 IMP:N=1 IMP:P=1
9 1 -0.00129 -11 -12 #15 #16 #17 #18  TRCL=2 IMP:N=1 IMP:P=1
10 6 -2.3 -13              TRCL=4 IMP:N=1 IMP:P=1
11 6 -2.3 -14              TRCL=5 IMP:N=1 IMP:P=1
12 6 -2.3 -15              TRCL=6 IMP:N=1 IMP:P=1
13 6 -2.3 -16              IMP:N=1 IMP:P=1
14 6 -2.3 -17              IMP:N=1 IMP:P=1
19 1 -0.00129 -10 #1 #2 #3 #4 #5 #6 #7 #8 #9 #10 #11 &
             #12 #13 #14 #15 #16 #17 #18 IMP:N=1 IMP:P=1
20 0 10                    IMP:N=0 IMP:P=0

1 RPP -13.5 6.5 -6.5 6.5 -6.5 6.5
2 RPP 6.5 16.66 -2.54 2.54 -2.54 2.54
3 RPP -23.66 16.66 -16.66 16.66 -16.66 16.66
4 RPP -33.82 26.82 -26.82 26.82 -26.82 26.82
5 RPP 26.82 29.36 -6.5 6.5 -6.5 6.5
6 RPP -2.5 2.5 -0.5 0.5 -2.5 2.5
7 CX 6.35
8 PX 6.35
9 PX -6.35
10 SO 1000
11 RPP -500 200 -90 90 -150 150
12 C/Y 0 -50 6.35
13 RPP -50 50 -100 100 -150 150
14 RPP -50 50 -150 150 -150 150
15 RPP -300 200 -50 50 -150 150
16 RPP -460 240 -270 210 150 250
17 RPP -460 240 -270 210 -450 -150
18 PY -75
19 PY 75
20 PY -90
21 PY 90
22 C/Y 0 -50 0.635
23 C/Y 0 -50 1.905
M1 &            $ AIR DENSITY = 0.001205 G/CC
6000 -0.000124 &
7014 -0.752290 &
7015 -0.002977 &
8016 -0.231153 &
```

```
8017 -0.000094 &
8018 -0.000535 &
18000 -0.012827
M2 &            $ LEAD DENSITY = 11.35 G/CC
82204 0.014000 &
82206 0.241000 &
82207 0.221000 &
82208 0.524000
M3 &            $ BORATED POLY DENSITY = 1.1 G/CC
1001 -0.1 &
6000 -0.6 &
5000 -0.3
M4 92238 1      $ DU DENSITY = 19.1 G/CC
M5 &            $ DENSITY = 0.92 G/CC
8000 0.802 &
1001 4.98 &
6000 2.87 &
5010 0.254
C
M6 &            $ CONCRETE ORDINARY DENSITY = 2.3 G/CC
1001.62C -0.022095 &
1002.24C -0.000005 &
6000.24C -0.002484 &
8016.62C -0.573373 &
8017.66C -0.000232 &
8018     -0.001326 &
11023.62C -0.015208 &
12000.62C -0.001266 &
13027.62C -0.019953 &
14028.24C -0.279872 &
14029.24C -0.014719 &
14030.24C -0.010036 &
19000.62C -0.010045 &
20000.62C -0.042951 &
26054.62C -0.000363 &
26056.62C -0.005914 &
26057.62C -0.000139 &
26058.62C -0.000019
*TR1 40 0 -50 45 135 90 -45 45 90 -90 -90 0
TR2 40 120 0
TR3 0 0 -50
TR4 190 -70 0
TR5 -410 -120 0
TR6 40 -220 0



MODE P N
SDEF POS = 40 230 -50
     VEC = 0 -1 0
     DIR = 1
     PAR = 2
```

```
     ERG = 22
PHYS:P 25 0 0 -1 0 -101 0
PHYS:N 100 0 0 -101 -1 0 0
ACT NONFISS=ALL
FCL:N 1
FCL:P 1
CUT:P J 0.1
CUT:N J 0.0001
F4:P 7
E4 1 1400I 6 T
NPS 1E9
```

REFERENCES

1. Gozani, T. *Active nondestructive assay of nuclear materials: principals and applications;* Technical Report; United States Regulatory Commission: Palo Alto, 1981.

2. Evaluated Nuclear Data File. www.nndc.bnl.gov/csewg/ (accessed January 28, 2014).

3. Alamaniotis, M.; Hernandez, H.; Jevremovic, T. Application of Support Vector Regression in Removing Poisson Fluctuation from Pulse Height Gamma-Ray Spectra. *Proceedings of the 4th international Conference on Information, Intelligence, Systems and Applications* , Piraeus, 2013; pp 18-21.

4. Amano, Y. *Nuclear Security Plan 2010-2013;* Board of Governors General Conference Agenda; International Atomic Energy Agency: Vienna, 2009.

5. Chichester, D. L.; Seabury, E. H. Using Electronic Neutron Generators in Active Interrogation to Detect Shielded Fissionable Material. *IEEE TRASACTIONS ON NUCLEAR SCIENCE* **2009,** *56* (2), 441-446.

6. Gozani, T. Fission Signatures for Nuclear Material Detection. *IEEE TRANSACTIONS ON NUCLEAR SCIENCE* **2009,** *56* (3), 736-741.

7. Reedy, E. T. E.; Thompson, S. J.; Hunt, A. W. The detection of delayed gamma-rays between intense bremsstrahlung pulses for discriminating fissionable form non-fissionable materials. *Nuclear Instruments and Methods in Physics Research A* **2009,** No. 606, 811-814.

8. Medalia, J. *Detection of Nuclear Weapons and Materials: Science, Technologies, Observations ;* technical ; Congressional Research Service, 2010.

9. Jones, J. L.; Yoon, W. Y.; Harker, Y. D.; Hoggan, J. M.; Haskell, K. J.; VanAusdein, L. A. *Proof-of-Concept Assesment of a Photofission Based Interrogation System for the Detection of Shielded Nuclear Material;* Proof-of-Concept; Idaho National Engineering and Environmental Laboratory: Idaho Falls, 2000.

10. Mihalczo, J. T. *Radiation Detection for Active Interrogaiton of HEU;* Technical ; Oak Ridge National Laboratory: Oak Ridge, 2004.

11. Wehe, D. K.; H., Y.; Jones, M. H. Observation of U238 Photofission Products. *IEEE Transactions on Nuclear Science* **2006,** *53* (3), 1430-1434.

12. Thornton, S. T.; Rex, A. *Modern Physics for Scientists and Engineers,* 3rd ed.; Thomson Brooks/ Cole: Belmont, 2006.

13. Reedy, E. *Discrete gamma-rays From Photofission for Nuclear Forensics Applications;* MS Thesis; Idaho State University : Pocatello, 2011.

14. Jevremovic, T. *Nuclear Principles in Engineering,* 2nd ed.; Springer Science+Business Media, LLC: West Lafayette, 2009.

15. Pozzi, S. A.; Mihalczo, J. T. Toward the Simulation of Photofission for Nuclear Material Identification. *Journal of Nuclear Materials Managment* **2005,** *34* (1), 38-47.

16. Brueckner, K. A.; Thieberger, R. Nuclear Giant Dipole Resonance. *Physical Review Letters* **1960,** *4* (9), 466-468.

17. Tsoulfanidis, N.; Landsberger, S. *Measurement and Detection of Radiation ,* 3rd ed.; CRC Press: Boca Raton, 2011.

18. Knoll, G. F. *Radiation Detection and Measurement,* 3rd ed.; John Wiley & Sons, Inc : New York, 2000.

19. Office of the General Counsel U.S. Nuclear Regulatory Commission. *Atomic Energy Act of 1954;* Nuclear Regulatory Legislation; Washington, 2013.

20. Norman, E. B.; Prussin, S. G.; Larimer, R.; Shugart, H.; Browne, E.; Smith, A. R.; McDonald, R. J.; Nitsche, H.; P., G.; Frank, M. I.; Gosnell, T. B. Signatures of fissile materials: high-energy gamma-rays following fission. *Nucelar Instruments and Methods in Physics Research A* **2003,** No. 521, 608-610.

21. Yang, H. *Active Interrogation Methods For Detection of Special Nuclear Material;* PhD Thesis; University of Michigan: Ann Arbor, 2009.

22. Dighe, P. M.; Goswami, A.; Das, D.; Mittal, K. C.; Pithawa, C. K. Quantification of fissionable materials in pure and mixed form using photofission. *Nuclear Instruments and Methods in Physics Research Section A* **2014,** *737,* 242-247.

23. Beddingfield, D. H.; F.E., C. Identification of fissile materials from fission product gamma-ray spectra. *Nuclear Instruments and Methods in Physics Research A* **1998,** *417,* 405-412.

24. Thierens, H.; De Frenne, D.; Jacobs, E.; De Clercq, A.; D'hondt, P.; Deruytter, A. J. Product Yields for the photofission of 235U and 238U with 25-MeV bremsstralung. *Physical Review C* **1976,** *14* (3), 1058-1067.

25. Naik, H.; Carrel, F.; Kim, G. N.; Laine, F.; Sari, A.; Normand, S.; Goswami, A. Mass yield distributions of fission products from photo-fission of U238 induced by 11.5-17.3 MeV bremsstrahlung. *The European Physical Jornal A* **2013,** *49* (94).

26. Carrel, F.; Gmar, M.; Laine, F.; Loridon, J.; Ma, J.-L.; Passard, C. Identification of Actinides Inside Nucelar Waste Packages by Measurement of Fission Delayed Gammas. *IEEE Nuclear Science Symposium Conference Record* , 2006; pp 909-913.

27. Ishkhanov, B. C.; Kuznetsov, A. A. The Mass Distribution of 238U Photofission Fragments. *Moscow Univeristy Physics Bulletin* **2013,** *68* (4), 279-287.

28. Naik, H.; Nimje, V. T.; Raj, D.; Suryanarayana, S. V.; Goswami, A.; Singh, S.; Acharya, S. N.; Mittal, K. C.; Ganesan, S.; Chandrachoodan, P.; Manchanda, V. K.; Venugopal, V.; Banarjee, S. Mass distribution in the bremsstralung-induced fission of 232Th, 238U and 240Pu. *Nuclear Physics A* **2011,** No. 853, 1-25.

29. Runkle, R. C.; Chichester, D. L.; Thompson, S. J. Rattling Nucleons: New developments in active interrogation of special nuclear material. *Nuclear Instruments and Methods in Physics Research A* **2012,** *663,* 75-95.

30. Pozzi, S. A.; Clarke, S. D.; Walsh, W. J.; Miller, E. C.; Dolan, J. L.; Flaska, M.; Wieger, B. M.; Enqvist, P. E.; Mattingly, J. K.; Chichester, D. L.; Peerani, P. MCNPX-PoliMi for nuclear nonproliferation applications. *Nuclear Instruments and Methods in Physics Research Section A* **2012,** *694,* 119-125.

31. Brown, F. B.; Martin, W. R. Monte Carlo Methods for Radiation Transport Analysis on Vector Computers. *Progress in Nuclear Energy* **1984,** *14* (3), 270-272.

32. Wen, X.; Kavouras, J. G.; Nakazawa, D. R.; Yang, H. Simulation and Measurement of Delayed gamma-rays After Photon-induced Fission. *Nuclear Instruments and Methods in Physics Research Section A* **2013**.

33. Durkee, J. . J. W.; James, M. R.; McKinney, G. W.; Trellue, H. R.; Waters, L. S.; Wilson, W. B. Delayed-gamma signature calculation for neutron-induced fission and activation using MCNPX. Part II: Simulations. *Progress in Nuclear Energy* **2009,** *51* (8), 828-836.

34. Francesc, S.; M, F.-V. J.; Sempau, J. *PENELOPE-2008: A Code System for Monte Carlo Simulation of Electron and Photon Transport;* Workshop Proceedings ; Nuclear Energy Agency: Barcelona, 2009.

35. Lux, I.; Koblinger, L. *Monte Carlo Particle Transport Methods: Neutron and Photon Calculations;* CRC Press: Budapest, 1991.

36. Padovani, E.; Monville, M.; Pozzi, S. Monte Carlo modeling of delayed nuetrons from photofission. *Nuclear Science and Engineering* **2007,** *155,* 131-142.

37. Wilcox, T.; Kawano, T.; McKinney, G. W.; Hendricks, J. S. Correlated gammas using CGM and MCNPX. *Progress in Nuclear Energy* **2013,** *63,* 1-6.

38. Van Criekingen, S. *Mixed-Hybrid Discretization Methods for the Linear Transport Equation;* PhD Thesis; Northwestern University: Evanston, 2004.

39. Spanier, J.; Gelbard, E. M. *Monte Carlo Principles and Neutron Transport Problems;* Addison-Wesley: Reading, 1969.

40. Yates, R. D.; Goodman, D. J. *Probability and Stochastic Processes ,* 2nd ed.; John Wiley & Sons, INC., 2004.

41. X-5 Monte Carlo Team. *MCNP- A General Monte Carlo N-Particle Transport Code, Version 5;* Users Manual ; Los Alamos National Laboratory: Los Alamos, 2008.

42. McKinney, G. W. Tally Tagging Feature in MCPNX 2.7.A. *ANS Winter Meeting*, Reno, 2008.

43. Durkee, J. . J. W.; James, M. R.; McKinney, G. W.; Trellue, H. R.; Waters, L. S.; Wilson, W. B. Delayed-gamma signature calculation for neutron-induced fission and activation using MCPNX, Part 1: Theory. *Progress in Nuclear Energy* **2009,** *51,* 813-827.

44. White, M. C. *A Brief Primer for Simulating Photonuclear Interactions with MCNP(X);* memorandum; Los Alamos National Laboratory: Los Alamos, 2001.

45. *MCNPX Version 2.7.0 User's Manual;* User's Manual; Los Alamos National Laboratory: Los Alamos , 2011.

46. Koning, A. J.; Rochman, D.; van der Marck, S. C.; Kopecky, J.; Sublet, J. C.; Pomp, S.; Sjostrand, H.; Forrest, R.; Bauge, E.; Henriksson, H. TENDL-2012: TALYS-based evaluated nuclear data library. ftp://ftp.nrg.eu/pub/www/talys/tendl2012/tendl2012.html (accessed March 18, 2013).

47. Sibczynski, P.; Kownacki, J.; Syntfeld-Kazuch, A.; Moszynski, M.; Kisielinski, M.; Czarnacki, W.; Kosinski, K.; Matusiak, M.; Klimasz, M.; Kowalczyk, M.; Abraham, T.; Mierzejewski, J.; Srebrny, J. Decay chains and photofission investigation based on nuclear spectroscopy of highly enriched uranium sample. *Applied Radiation and Isotopes* **2013,** *82,* 170-174.

48. Campbell, L.; Misner, A.; Smith, E. L.; Reese, S.; Robinson, J. *High-energy Delayed Gamma Spectroscopy for Plutonium Assay of Spent Fuel;* Technical ; Pacific Northwest National Laboratory, International Atomic Energy Agency, Oregon State University: Richland, Vienna, Corvallis , 2010.

49. Baumung, K.; Bohnel, K.; Klunker, J.; Kuchle, M.; Wolff, J. Investigations into nondestructive safegaurds techniques. *IAEA Symposium on Safeguards Techniques*, Karlsruhe, 1970; p 192.

50. General Atomics. *Application of photo induced reactions to nuclear materials safeguards problems;* GA-9614; San Diego, 1969.

51. Reilly, D.; Ensslin, N.; Smith, H. J. *Passive Nondestructive Assay of Nuclear Materials;* Los Alamos, 1991.

52. Gmar, M.; Capdevila, J. M. Use of delayed gamma spectra for detection of actinides (U,Pu) by photofission. *Nuclear Instruments and Methods in Physics Research A* **1999,** *422,* 841-845.

53. Ishkhanov, B. S.; Kuznetsov, A. A. Photofission of 238U at the Energy of the Giant Dipole Resonace. *Moscow University Physics Bulletin* **2012,** *68* (1), 27-33.